Numerical Heat Transfer- Part A: Applications

https://www.tandfonline.com/toc/unht20/current

Accepted December 21st 2023

Ternary Cobalt ferrite ($CoFeO_4$) -Silver (Ag) -Titanium dioxide (TiO_2) hybrid nanofluid hydromagnetic non-linear radiative-convective flow from a rotating disk with viscous dissipation, non-Darcy and non-Fourier effects: *Swirl coating simulation*

[1]M. Gnaneswara Reddy, [1]K. Bhagya Swetha Latha, [2]D. Tripathi*, [3]O. Anwar Bég, [3]S. Kuharat and [3]Martin L. Burby

[1]*Department of Mathematics, Acharya Nagarjuna University Campus, Ongole - 523 001, A.P., India,* mgrmaths@gmail.com, drmgranu@gmail.com

[2]*Department of Mathematics, National Institute of Technology, Uttarakhand-246174,* **India.**

[3]*Multi-Physical Engineering Sciences Group, Dept. Mechanical and Aeronautical Engineering, Corrosion/Coatings Lab, 3-08, SEE Building, Salford University, Manchester, M54WT,* **UK.** O.A.Beg@salford.ac.uk; S.Kuharat2@salford.ac.uk; M.Burby@salford.ac.uk

*Corresponding author E-mail: *dtripathi@nituk.ac.in*

ABSTRACT

Magnetic nanoparticles are increasingly being deployed in smart coating systems due to their exceptional functionalities and abilities to be tuned for specific environmental conditions. Inspired by the emergence of tri-hybrid magnetic nanofluids which utilize three distinct nanoparticles in a single base fluid coating, the present article examines analytically and computationally the swirl coating of magnetic ternary hybrid nanofluid from a rotating disk, as a simulation of spin coating deposition processes in materials manufacturing. Owing to high temperature fabrication conditions, thermal radiative heat transfer is also considered and a Rossleand flux model deployed. $CoFeO_2$-Ag-TiO_2 hybrid nanoparticles are considered with Ethylene Glycol-Water ($C_2H_6O_2 - H_2O$ 40: 60%) base fluid. A filtration medium is also featured (porous medium) adjacent to the disk and the Darcy-Forchheimer model is deployed to simulate both bulk matrix porous drag encountered at lower Reynolds numbers and inertial quadratic drag generated at higher Reynolds numbers. Thermal relaxation of the coating nanofluid is additionally addressed and a non-Fourier Cattaneo-Christov model is therefore implemented in the heat conservation equation. Viscous dissipation is also included in the model. The governing conservation equations for mass, momenta (radial, tangential and axial) and energy with prescribed boundary conditions are rendered into coupled nonlinear ordinary differential boundary layer equations via suitable scaling variables and the Von Karman transformations. The derived reduced boundary value problem is then solved with a Runge-Kutta numerical scheme and shooting scheme in

MATLAB. Validation of solutions is included with previous studies. Radial and azimuthal velocities, temperature, radial skin-friction, azimuthal skin friction and local Nusselt number are computed for a range of selected parameters. A comparative assessment of mono nanofluid $CoFeO_2$, Hybrid $CoFeO_2$-Ag nanofluid and tri-hybrid $CoFeO_2$-Ag-TiO_2 nanofluid is conducted. This combination of hybrid nanoparticles has never been examined previously in the literature and constitutes the significant novelty of the present work. Both radial and tangential velocity are depleted with increasing applied magnetic field whereas temperature and thermal boundary layer thickness are increased.

KEYWORDS: *Cattaneo-Christov heat flux; non-linear radiation; dissipation; Darcy-Forchheimer model; ternary hybrid ($CoFeO_2 - Ag - TiO_2$) nanofluid; MHD; rotating disk; spin coating; functional materials.*

1. INTRODUCTION

The transport from a rotating disk is a fundamental topic in fluid dynamics and features in many diverse applications including rotating disk cathodes, rotor aerodynamics, bioreactors and spin coating in materials processing. The flow of a Newtonian fluid from a rotating disk surface was first addressed theoretically by Von Karman [11] who reduced the Navier-Stokes equations to a set of coupled ordinary differential equations via carefully selected coordinate transformations and provided a robust platform for obtaining solutions for the radial, tangential and axial velocity fields and also pressure distribution. Important fundamental studies on Newtonian viscous swirling flows were subsequently communicated by Cochran [2], Stuart [3] (who considered disk transpiration) and Gregory *et al.* [4]. Further investigations were reported by Beton [5] (using asymptotic expansion), Mehmood *et al.* [6] (on transient effects for rotor disk applications with a homotopy method), Balachandar and Streett [7] (on transition from laminar to turbulent flow), Kelson, and A. Desseaux (who considered the existence of solutions for different wall suction conditions), and Jasmine and Gajjar [9] (who deployed spectral methods and a linear stability analysis to examine the impact of variable viscosity on momentum and thermal transport characteristics). In industrial materials processing systems, the deposition of a thin liquid film over a horizontal rotating disk by the action of the centrifugal force is termed *spin coating*. This technique is widely used in the manufacture of for example integrated circuits, sensor fabrication and emerging complex functional coatings [10, 11]. The complex nature of spin coating invokes many multi-physical phenomena including time-dependent effects, heat transfer, species diffusion, magnetohydrodynamics (MHD), thermocapillary (Marangoni) surface tension, non-Newtonian behaviour and combinations of these effects. This has motivated many researchers to significantly extend the fundamental Von Karman swirl flow problem to more accurately represent the complexities of spin coating. In particular in *magnetic spin coating*, which is appropriate for electro-conductive liquids, the use of an external magnetic field has been shown to be very effective in balancing the centrifugal force for coating homogeneity via regulation of the film thickness [12]. By varying the magnetic field, radial and tangential velocity distributions can also be manipulated very dramatically [13]. The distribution of particles in coatings can also be modified via a careful prescription of magnetic field intensity, which has proven instrumental in for example solar cell coatings utilizing lead iodide [14]. The robust simulation of magnetic field effects on viscous swirling flows requires MHD (magnetohydrodynamic) models. These have been developed extensively for a variety of coating flow scenarios. Some important contributions in this regard are the works of Sparrow and Cess [15] (which includes convective heat transfer). Kakutani [16] showed that for an axial magnetic field, the torque due to viscous friction is boosted with magnetic interaction parameter whereas the boundary layer displacement-thickness and the yaw angle far from the disk surface are depleted. Further investigations include Pao [17] who showed numerically that for a circular magnetic field, with stronger intensity the boundary layer thickness is enhanced, axial flow is decelerated, and very high magnetic field may even induce flow separation. More recent investigations include Turkyilmazoglu [18, 19] who computed the effect of an axial magnetic field on the resonances in swirling magnetic disk flow leading, respectively, to the direct spatial instability, the direct temporal instability and the absolute instability.

The above studies considered purely fluent electromagnetic media. In recent years, with developments in flow control in materials processing and also hybrid bioreactors, porous media have been explored widely. A porous medium comprises a bulk matrix structure with voids which permit the percolation of fluid. The random distribution of voids implies a heterogenous structure which is very difficult to analyse even with advanced computer hardware. A more pragmatic approach is to average the porosity over a volume and consider drag force effects. The classical approach for this is the Darcy model which assumes that flux through the porous medium is proportional to pressure gradient and permeability of the porous medium (hydraulic conductivity) but inversely proportional to dynamic viscosity and the length percolated. This model is appropriate for low Reynolds numbers. However, at larger Reynolds numbers (as encountered in some spin coating systems), while still laminar, higher order drag effects are induced. A more suitable formulation for simulating these effects is the Darcy-Forchheimer quadratic model. This "non-Darcy" methodology has been deployed in many swirling and other flow problems in porous media. In these studies, the anisotropy of the porous medium has also been simplified to consider a single permeability in all directions, which is distinct from the porosity of the medium (i.e. ratio of the volume of voids to the total volume of the porous medium). Furthermore, the porous medium has been assumed (correctly) to be completely saturated with fluid i. e. absence of air in the voids. Nakayama and Ebinuma [20] investigated unsteady convection from an isothermal wall adjacent to a non-Darcy porous medium. They showed that Forchheimer drag decelerates the flow and also delays both the time required to attain steady state conditions and the spreading of the thermal boundary layer over the wall surface. Bég *et al.* [21] deployed an electrothermal network solver (PSPICE) to compute the unsteady viscous flow in a rotating channel containing Darcy-Forchheimer porous media. They showed that with elapse in time and increment in Darcy number, the primary flow is accelerated whereas an increment in Forchheimer number strongly decelerates both primary and secondary flow. They also noted that a boost in Ekman number (ratio of the viscous force in the fluid to the Coriolis force) strongly damps the secondary flow. Electromagnetic (EMHD) viscoelastic convective flow in non-Darcy porous media has been studied very recently by Fasheng *et al*. [22] with a differential transform method (DTM) and a Brinkmann-extended Darcy-Forchheimer. They showed that strong flow retardation is produced with elevation in the Forchheimer number whereas higher values of this parameter, Hartmann (magnetic) parameter and Darcy number all enhance the wall heat transfer rate (average Nusselt number). Several researchers have also considered Von Karman swirling flow in porous media. Attia [23] and Rashidi *et al*. [24] both employed a Darcian model to consider steady thermal convection from a rotating disk. Bég *et al.* [21] presented the first theoretical study of polymer swirling flow from a rotating disk to a Darcy-Forchheimer porous medium. They showed that both radial and tangential velocity components are increased with increasing Darcy number whereas they are both suppressed with increasing Forchheimer number, for both pseudoplastic and dilatant fluids. All these studies confirmed the tangible impact of second order Forchheimer drag in porous media transport modelling.

A major motivation for the present study is novel functional materials processing. In spin coating operations, often very high temperatures are required to produce the desired consistency in coatings. Therefore, in addition to thermal conduction at the rotating disk and thermal convection in the swirling fluid, *radiative heat transfer* is also invoked [26]. This is the most complex mode of heat transport and as such has often been neglected in previous analytical investigations. Optical properties of the coating fluid are required for accurate simulations [27] and additionally the formidable integro-differential equation of radiation heat transfer must be accommodated. Many more pragmatic approaches have been developed to circumvent the need to solve this equation. These generally fall under the umbrella of algebraic flux models and include the Schuster-Schwartzchild two-flux model, the Hamaker six flux model, the Traugott P1 differential approximation and Chandrasekhar's discrete ordinates model (DOM). However, these models still necessitate the solution of additional equations to the convective-conductive energy balance equation, as elaborated in succinct detail by Bergman and Viskanta [28]. A simpler but reasonably accurate model for radiative flux is the Rosseland diffusion flux model which modifies the energy equation with an augmented thermal diffusion for the radiative flux. This model has therefore understandably emerged as the most popular in multi-physical fluid dynamics, although it is limited to optical thickness values of about 5 and cannot simulate scattering effects. However, it does approximate quite well the absorbing and emitting characteristics of a range of coating materials. Bég *et al.* [29] applied the Rosseland diffusion flux model in MHD Von Karman swirling flow from a perforated rotating disk with wall slip and variable thermophysical properties. They used the computational network solver PSPICE and observed that only the axial velocity component is suppressed with greater radiative flux (there is no modification in radial and tangential velocities) whereas temperature and thermal boundary layer thickness are substantially elevated.

The above studies which considered heat transfer have been confined to the classical Fourier theory of heat conduction. This model uses a *parabolic-type* partial differential equation which implies an infinite speed for heat transport which is not physically realistic. Since Fourier's law does not predict finite wave speeds, it fails to represent certain applications in for example materials processing systems where instantaneous energy transmission occurs in a short duration or when the thermal propagation speed is not high. Cattaneo [30] modified the Fourier model to produce a *hyperbolic-type* heat transport equation which successfully predicts finite speed for heat transport. In this model, which is also known as the Cattaneo-Christov model, heat transport is considered as a wave phenomenon rather than a diffusion phenomenon and sometimes termed "second sound". Özisik and Tzou [31] further demonstrated that hyperbolic heat conduction is more precise when considering porous media e. g. metallic foams, which feature in materials fabrication technologies. Other relevant applications include modulated laser processing [32], radiative coating [33], thermal spray deposition and welding [34-35] and thermal surface finishing [36]. The hyperbolic heat conduction equation based on the Cattaneo-Christov model for the heat flux features a thermal relaxation mechanism which can accommodate the gradual modification in the temperature gradient. In the context of external boundary layer flows (of relevance to coating and enrobing), several authors have utilized the Cattaneo-Christov model. Alamari *et al.* [37] considered the thermo-solutal non-Newtonian convection from an extending cylindrical body with magnetic field and non-Fourier heat flux effects. Shehzad *et al.* [38] computed the viscoelastic convective flow in non-Darcy porous media with the Cattaneo-Christov heat flux and also variable conductivity effects. They utilized a modified non-Fourier Deborah number and showed that higher values of this parameter reduce temperature and also thermal and momentum boundary layer thickness. Non-Fourier von karman swirling flows have also been addressed recently. Hafeez *et al.* [39] considered magnetized flow of an Oldroyd-B fluid from a rotating disk and observed that increasing thermal relaxation time both decelerates the radial and tangential flow and cools the regime i.e. decreases thermal boundary layer thickness. Misha *et al.* [40] studied the dual disk Von Karman flow non-Fourier swirling heat transfer problem with a Van Dyke perturbation method. They showed that with higher non-Fourier (thermal relaxation) parameter, the heat transfer rate to the disk surfaces (Nusselt number) is suppressed and that the Fourier model significantly under-predicts temperatures within the viscous fluid.

Conventional working fluids deployed in for example coatings as glycol, polymer, water, ethylene and oil have small thermal conductivities. In order to improve the thermal transport capacity in these regular fluids, a new technology of *nanoscale-engineering fluids* has emerged. Known as *nanofluids,* this breakthrough was initiated by Choi [41] in 1995 for the enhancement thermal performance in the fluids. The excellent heat transfer properties of nanofluids were confirmed in many subsequent experimental studies using a variety of different metallic and metallic oxide nanoparticles in combination with different working fluids [42-45]. The agglomeration (clustering) of nanoparticles was found to be minimal at optimized volume fractions, usually less than 10%. Mathematical models of nanofluid transport were later developed to explain the experimental observations and included the Buongiorno two-component model and the group of volume fraction models including Tiwari-Das, Maxwell–Garnett and Patel models. Many of these studies have been summarized in Kumar and Subudhi [46], although not for swirling flows. Bachok *et al.* [47] presented one of the first studies of

Von Karman swirling flow of nanofluids using the Maxwell–Garnett and Patel models. They considered three different nanoparticles - Copper (Cu), Titanium dioxide (TiO_2) and Aluminium oxide (Al_2O_3), suspended in water (H_2O) base fluid and observed that heat transfer rate to the disk is diminished with greater nanoparticle volume fraction and that higher temperatures are achieved in the boundary layer with copper. Andrews and Devi [48] considered only copper-water nanofluid. Rashidi *et al.* [49] considered magneto-convective swirl flow of Cu/CuO/Al_2O_3-water nanofluid from a porous rotating disk. Further studies were communicated by Yin *et al.* [50] again for Cu/CuO/Al_2O_3-water nanofluid and Ahmed *et al.* [51] for magnetic nanofluid swirling flow with thermophoresis and Brownian diffusion effects (not specific nanoparticles). Radiative heat transfer in swirling nanofluid flows were studied by Khan *et al*. [52, 53], Upadhya *et al.* [54] and Alsallami *et al*. [55]. These works showed that combining radiative heat flux with appropriate nanoparticle volume fractions is also a very potent mechanism for boosting heat transfer rates. More recently Von Karman swirling flows in non-Darcy permeable media were examined by Umavathi and Bég [56] for unitary nanofluids and by Bég *et al.* [57] for micro-organism-doped nanofluids. It was shown in these analyses that combining porous media with nanoparticle volume fractions is equally effective at manipulating thermal efficiency in rotating disk coating flows. All the above investigations have generally confirmed that with selected unitary nanoparticles (metallic or oxide) and optimum doping percentages the heat transfer characteristics can be manipulated successfully.

The thermal enhancement for mono-nanofluid (unitary nanofluid) has however been shown to be superseded by hybrid nanofluid (binary composite nanofluid). Hybrid nanofluids are prepared by suspending two non-identical nanoparticles in a base liquid. These fluids have exhibited substantial improvements in thermal efficiency relative to unitary nanofluids. Kumar *et al.* [58] studied Darcy–Forchheimer flow of Casson hybrid nanofluid (comprising Graphene oxide and Titanium dioxide nanoparticles in 50% Ethylene glycol base fluid) from a vertically upward/downward moving rotating disk. Tassaddiq *et al.* [59] considered swirling flow of $CNT + Fe_3O_4/H_2O$ hybrid nanofluid. Shoaib *et al.* [60] considered Cu and Al_2O_3-water hybrid nanofluids in rotating hydromagnetic channel flow with radiation heat transfer, wall slip and nanoparticle shape factor effects. Waqas *et al.* [61] examined SWCNT-Titania/MWCNT-Cobalt ferrous oxide-water hybrid nanofluids in magnetized rotating disk flow with radiative flux. Further investigations exploring different nanoparticle combinations in hybrid (binary) nanofluids include Ijaz Khan *et al.* [62] (Aluminium oxide (Al_2O_3) + Copper(Cu) nanoparticles), Kumar and Mondal [63] (Cu -Al_2O_3-water nanofluids) and Mousavi *et al.* [64]

(Zinc Oxide-Ag nanoparticles). A further refinement in nanofluids is the ternary (tri-hybrid) nanofluid, which combines three distinct nanoparticles disseminated into a single base fluid. This constitutes the latest development in nanofluid technology. Several interesting simulations of ternary nanofluids in Von Karman swirling flows have been presented recently. Heat transfer characteristics of tri-hybrid $CuO - Al_2O_3$-Cu -water nanofluid from a spinning disk was scrutinized by Shahzad *et al.* [65]. Alshahrani *et al*. [66] computed the steady swirling flow of tri-hybrid CNTs- Zirconium (ZrO_2)-Aluminum oxide (Al_2O_3) nanofluids observing a substantial boost in temperature compared with dual (binary) or unitary nanofluids. Shamshuddin *et al.* [67] studied Copper (Cu)-Iron oxide (Fe_3O_4)-Silicon dioxide (SiO_2) -polymer ternary hybrid nanofluid flow from a spinning disk with radiative heat transfer. Other works of relevance include Mustafa *et al.* [68], Acharya *et al.* [69], Waini *et al.* [70] and Khan *et al.* [71].

The principal objective of the current investigation is to analyse the Von Karman swirling flow of magnetic ternary hybrid ($CoFeO_4$-Ag-TiO_2), hybrid ($CoFeO_4$-Ag) and unitary ($CoFeO_4$) - $C_2H_6O_2$-H_2O $40{:}\,60\%$ nanofluids from a rotating disk to a non-Darcy porous medium, as a simulation of multi-functional spin nano-coating manufacture [72-76]. The present work also extends the existing literature with several novelties, namely the inclusion of viscous dissipation, non-Fourier Cattaneo-Christov heat flux, Darcy-Forchheimer drag force and also non-linear radiative heat flux effects. The governing conservation equations for mass, momenta (radial, tangential and axial) and energy with prescribed boundary conditions are transformed into a nonlinear coupled ordinary differential boundary value problem via appropriate scaling variables and the Von Karman transformations. A numerical solution is presented using the Runge-Kutta method and a shooting scheme in MATLAB. Validation of solutions is included with previous studies. Radial and azimuthal velocities, temperature, radial skin-friction, azimuthal skin friction and local Nusselt number are computed for a range of selected parameters and visualized graphically with detailed interpretation. The present study constitutes a significant extension to the existing literature on magnetic hybrid nanofluid spin coating simulation. In particular, it addresses novel emerging hybrid ternary nanofluids which combine the thermal conductivity and electromagnetic functionality of three nanoparticles enabling fine tuning under applied magnetic fields. Iron oxide and cobalt-ferrous oxides have been shown to produce electro-active phase ability and are therefore also combined with silver and titanium dioxide in this work as these other nanoparticles offer anti-bacterial and excellent high temperature performance. Cobalt also has demonstrated excellent anti-corrosion properties and is resilient and durable. These multi-structured nanofluids offer some significant advantages for "smart" coatings as they combine the separate advantages of unitary nanoparticles without adverse interactions [72, 73].

2. MATHEMATICAL TERNARY HYBRID MAGNETIC NANOFLUID SWIRL MODEL

Steady incompressible boundary layer swirling coating flow of dissipative magnetic tri-hybrid ($CoFeO_4$-Ag-TiO_2) nanofluid in a cylindrical coordinate system (r, φ, z), from a rotating disk spinning with constant angular velocity, Ω about the z −axis, adjacent to a homogenous, isotropic, non-deformable porous (filtration) medium, under static axial magnetic field, B_o, is examined. The Darcy-Forchheimer drag force model is deployed for the porous medium. Three metallic nanoparticles - Cobalt ferrite ($CoFeO_4$), Silver (Ag), Titanium dioxide (TiO_2) - are utilized and a mixture of 40 % Ethylene ($C_2H_6O_2$) and 60% water (H_2O) is employed as the base (coating) fluid. The velocity components (u, v, w) correspond to the coordinates (r, φ, z). The temperature is sufficiently high to invoke radiative flux. Viscous dissipation and non-Fourier heat flux are also considered. **Fig.1** visualizes the regime.

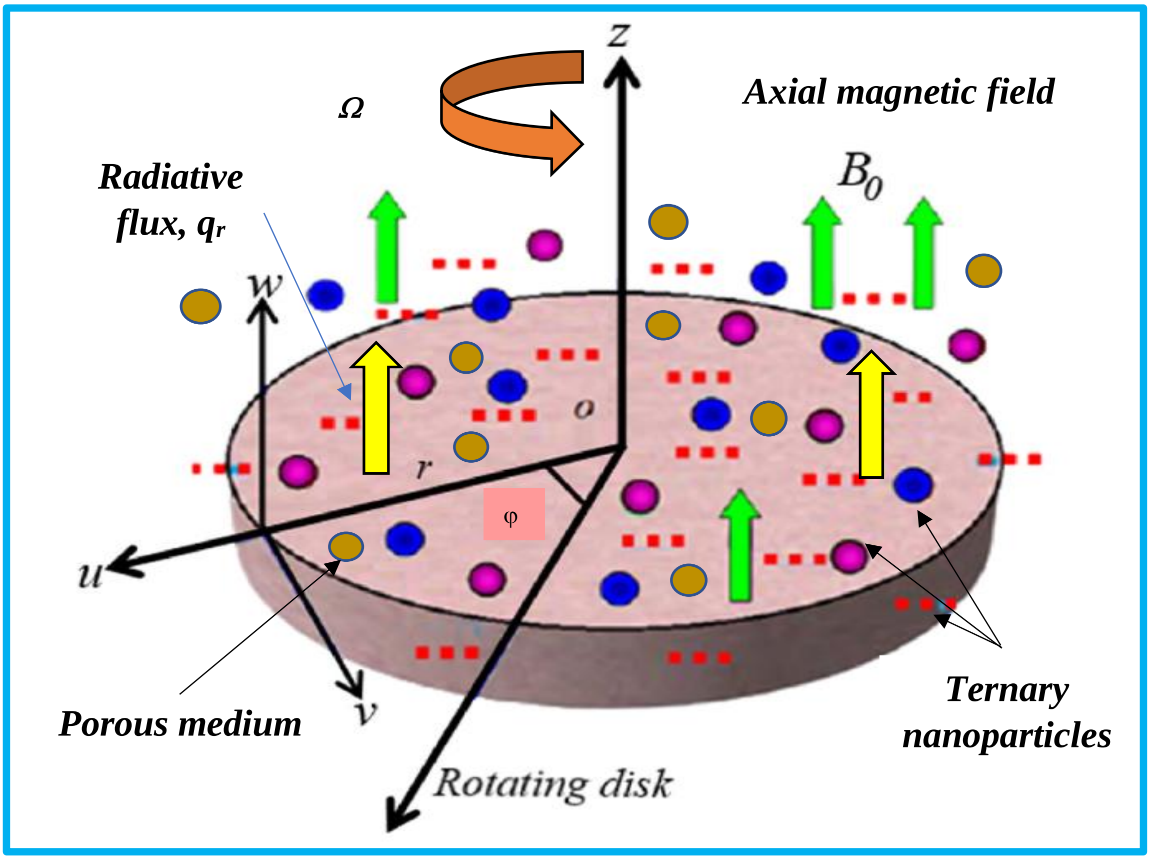

Fig.1. Physical flow configuration.

The disk surface is solid and electrically insulated and Hall current and magnetic induction effects are neglected. It is assumed that the disk temperature at the surface and away from the disk are respectively, T_w and T_∞. Based on the above assumptions, the governing flow equations for continuity, momentum and energy are obtained by amalgamating and extending the models in [24, 47, 49 and 61]:

$$\frac{\partial u}{\partial r}+\frac{u}{r}+\frac{\partial w}{\partial z}=0 \tag{1}$$

$$u\frac{\partial u}{\partial r}-\frac{v^2}{r}+w\frac{\partial u}{\partial z}+\frac{1}{\rho_{thnf}}\frac{\partial P}{\partial r} = \vartheta_{thnf}\left(\frac{\partial^2 u}{\partial r^2}+\frac{1}{r}\frac{\partial u}{\partial r}-\frac{u}{r^2}+\frac{\partial^2 u}{\partial z^2}\right)-\vartheta_{thnf}\frac{u}{K^*}-Fru^2 - \frac{\sigma_{thnf}}{\rho_{thnf}}B_0^2 u \tag{2}$$

$$u\frac{\partial v}{\partial r}+\frac{uv}{r}+w\frac{\partial v}{\partial z} = \vartheta_{thnf}\left(\frac{\partial^2 v}{\partial r^2}+\frac{1}{r}\frac{\partial v}{\partial r}-\frac{v}{r^2}+\frac{\partial^2 v}{\partial z^2}\right)-\vartheta_{thnf}\frac{v}{K^*}-Frv^2 - \frac{\sigma_{thnf}}{\rho_{thnf}}B_0^2 v \tag{3}$$

$$u\frac{\partial w}{\partial r}+w\frac{\partial w}{\partial z}+\frac{1}{\rho_{thnf}}\frac{\partial P}{\partial z}=\vartheta_{thnf}\left(\frac{\partial^2 w}{\partial r^2}+\frac{1}{r}\frac{\partial w}{\partial r}+\frac{\partial^2 w}{\partial z^2}\right)-\vartheta_{thnf}\frac{w}{K^*}-Frw^2 \tag{4}$$

$$(\rho c_p)_{thnf}\left(u\frac{\partial T}{\partial r}+w\frac{\partial T}{\partial z}\right) - \varepsilon_t\left[u^2\frac{\partial^2 T}{\partial r^2}+2vw\frac{\partial^2 T}{\partial r\partial z}+w^2\frac{\partial^2 T}{\partial z^2}+u\frac{\partial w}{\partial r}\frac{\partial T}{\partial z}+u\frac{\partial u}{\partial r}\frac{\partial T}{\partial r} + w\frac{\partial u}{\partial z}\frac{\partial T}{\partial z}+w\frac{\partial w}{\partial z}\frac{\partial T}{\partial z}\right] = k_{thnf}\left(\frac{\partial^2 T}{\partial r^2}+\frac{1}{r}\frac{\partial T}{\partial r}+\frac{\partial^2 T}{\partial z^2}\right)-\frac{\partial q_r}{\partial z}+\mu_{thnf}\left[\left(\frac{\partial u}{\partial z}\right)^2+\left(\frac{\partial v}{\partial z}\right)^2\right] \tag{5}$$

The prescribed boundary conditions at the disk surface (wall) and in the free stream are [24, 62] are:

$$u = 0,\ v = \Omega \mathrm{r},\ w = 0,\ T = T_w \ \text{at}\ z = 0$$
$$u \to 0,\ v \to 0,\ T \to T_\infty \ \text{as}\ z \to \infty \tag{6}$$

Here ρ_{thnf} , $\vartheta_{thnf} = \frac{\mu_{thnf}}{\rho_{thnf}}$, σ_{thnf} , $(\rho c_p)_{thnf}$, k_{thnf} , represent the density, kinematic viscosity, electrical conductivity, heat capacitance and thermal conductivity of tri-hybrid nanofluid, the fluid temperature, K^* is the isotropic permeability of the porous medium, ε_t is the Cattaneo-Christov thermal relaxation time, q_r is the radiative heat flux, Fr is the Forchheimer quadratic inertia coefficient of the porous medium.

The radiative heat flux q_r of the thermal radiation is given by the Rosseland diffusion approximation [29, 61, 62]:

$$q_r = -\frac{4}{3}\frac{\sigma^*}{k^*}\frac{\partial T^4}{\partial z} = -\frac{16}{3}\frac{T_\infty^3}{k^*}\frac{\partial T}{\partial z} \tag{7}$$

Here σ^* denotes the Stefan-Boltzmann constant and k^* is the mean absorption coefficient.

The thermo-physical properties of the Cobalt ferrite ($CoFeO_4$), Silver (Ag), Titanium dioxide (TiO_2) nanoparticles and the Ethylene-Water 40:60% base fluid, are documented in **Table 1** and extracted from Khan *et al.* [71].

Table-1: Thermo-physical characteristics of three distinct nanoparticles and base fluid [71].

Physical characteristics	$CoFeO_4$	Ag	TiO_2	Ethylene Glycol EGW (40:60%)
ρ	4907	10.5	4250	1041.89
c_p	700	235	686.2	3421.54
σ	$5.51\text{x}10^{9}$	$3.6\text{x}10^{7}$	$2.38\text{x}10^{6}$	$5.5\text{x}10^{-6}$
k	3.7	429	8.9538	0.1816

The mathematical relations for the thermophysical properties for unitary nanofluid, hybrid binary nanofluid and ternary hybrid (tri-hybrid) nanofluid are as follows [67, 69, 71]:

$$\mu_{tnf} = \frac{\mu_f}{(1-\phi_1)^{2.5}(1-\phi_2)^{2.5}(1-\phi_3)^{2.5}},$$

$$\rho_{tnf} = (1-\phi_3)\left[(1-\phi_2)\left\{(1-\phi_1)\rho_f + \phi_1\rho_{s1}\right\} + \phi_2\rho_{s2}\right] + \phi_3\rho_{s3},$$

$$(\rho c_p)_{tnf} = (1-\phi_3)\left[(1-\phi_2)\left\{(1-\phi_1)\left(\rho c_p\right)_f + \phi_1\left(\rho c_p\right)_{s1}\right\} + \phi_2\left(\rho c_p\right)_{s2}\right] + \phi_3\left(\rho c_p\right)_{s3},$$

$$\frac{\sigma_{tnf}}{\sigma_{hnf}} = \frac{(1+2\phi_3)\sigma_{s3} + (1-2\phi_3)\sigma_{hnf}}{(1-\phi_3)\sigma_{s3} + (1+\phi_3)\sigma_{hnf}},$$

$$\frac{\sigma_{hnf}}{\sigma_{nf}} = \frac{(1+2\phi_2)\sigma_{s2} + (1-2\phi_2)\sigma_{nf}}{(1-\phi_2)\sigma_{s2} + (1+\phi_2)\sigma_{nf}},$$

$$\frac{\sigma_{nf}}{\sigma_f} = \frac{(1+2\phi_1)\sigma_{s1} + (1-2\phi_1)\sigma_f}{(1-\phi_1)\sigma_{s1} + (1+\phi_1)\sigma_f},$$

$$\frac{k_{tnf}}{k_{hnf}} = \frac{k_{s3} + 2k_{hnf} - 2\phi_3\left(k_{hnf} - k_{s3}\right)}{k_{s3} + 2k_{hnf} + \phi_3\left(k_{hnf} - k_{s3}\right)}, \tag{8}$$

$$\frac{k_{hnf}}{k_f} = \frac{k_{s2} + 2k_{nf} - 2\phi_2\left(k_{nf} - k_{s2}\right)}{k_{s2} + 2k_{nf} + \phi_2\left(k_{nf} - k_{s2}\right)},$$

$$\frac{k_{nf}}{k_f} = \frac{k_{s1} + 2k_f - 2\phi_1\left(k_f - k_{s1}\right)}{k_{s1} + 2k_f + \phi_1\left(k_f - k_{s1}\right)}$$

Here ϕ_1, ϕ_2 and ϕ_3 are the solid volume fractions of the three distinct nanoparticles.

To render the partial differential boundary value problem defined by Eqns. (1)-(6) as dimensionless, the following similarity transformations and non-dimensional variables are introduced [47, 62]:

$$u = r\Omega\frac{df}{d\zeta}, v = r\Omega \mathrm{g}(\zeta), w = -2\sqrt{\Omega\vartheta_f}\ \mathrm{f}(\zeta), \zeta = \sqrt{\frac{2\Omega}{\vartheta_f}}z, P = P_\infty + 2\Omega\mu_f\ \mathrm{f}(\zeta)$$

$$\lambda = \frac{\vartheta_f}{\Omega \mathrm{K}^*}, M = \frac{\sigma_f B_0^2}{\rho_f\Omega}, Fr = \frac{C_b}{rk^{*1/2}}, \theta(\zeta) = \frac{T-T_\infty}{T_w - T_\infty}, Pr = \frac{\vartheta_f}{\alpha_f}, Ec = \frac{r^2\Omega^2}{T_w},$$

$$Rd = \frac{16\sigma^* T_\infty^3}{3k^* k_f}, \Gamma_t = \varepsilon_t\Omega, T = T_\infty(1 + (\theta_w - 1)\theta), \theta_w = \frac{T_w}{T_\infty} \tag{9}$$

By making using equations (9) and (7), it is evident that the equation (1) is satisfied automatically and equations (2) - (6) are reduced to the following dimensionless ordinary differential equations:

$$\frac{N_1}{N_2}f''' + 2ff'' + g^2 - \lambda f' - (1+Fr)f'^2 - \frac{N_3}{N_2}Mf' = 0 \tag{10}$$

$$\frac{N_1}{N_2}g'' + 2fg' + g^2 - 2f'g - \lambda g - Frg^2 - \frac{N_3}{N_2}Mg = 0 \tag{11}$$

$$\theta'' + RdN_4\frac{d}{d\zeta}\left([1 + \theta(\zeta)(\theta_w - 1)]^3\, \theta'(\zeta)\right) + 2N_4N_5Prf\theta' - Pr\Gamma_t(f^2\theta'' + ff'\theta') + \frac{N_1}{N_5}\mathrm{Pr}\, Ec[(f'')^2 + (g')^2] = 0 \tag{12}$$

The transformed boundary conditions (6) become:

$$f = 0, f' = 0, g = 1, \theta = 1 \text{ at } \zeta = 0 \tag{13}$$
$$f' \to 0, g \to 0, \theta \to 0 \text{ as } \zeta \to \infty$$

Here ζ is scaled axial similarity coordinate (dimensionless), P is hydrodynamic pressure, M is the magnetic interaction parameter (ratio of Lorentz magnetic force to Coriolis force), $f'(\zeta)$ is dimensionless radial velocity function, $g(\zeta)$ is dimensionless azimuthal velocity function, $\theta(\zeta)$ is dimensionless temperature function, P_∞ is free stream pressure, λ is the inverse permeability parameter, Pr is the Prandtl number, Rd is the thermal radiation parameter, Ec is the Eckert number, θ_w is the temperature ratio parameter, Fr is the Forchheimer number, Γ_t is the non-Fourier thermal relaxation time and N_1, N_2, N_3, N_4 and N_5 are nanofluid property constants defined as follows:

$$N_1 = \frac{\mu_{thnf}}{\mu_f}, N_2 = \frac{\rho_{thnf}}{\rho_f}, N_3 = \frac{\sigma_{thnf}}{\sigma_f}, N_4 = \frac{k_f}{k_{thnf}}\ , N_5 = \frac{(\rho c_p)_{thnf}}{(\rho c_p)_f} \tag{114}$$

In the present model, if we choose the volume fraction of TiO_2 nanoparticle as $\phi_3 = 0$ then the model is reduced to hybrid binary $CoFeO_4$-Ag nanofluid model. Setting the volume fractions of Ag and TiO_2 nanoparticles as $\phi_2 = \phi_3 = 0$ then the current model is reduced to the $CoFeO_4$ unitary nanofluid model.

Key physical quantities of interest at the disk surface for nano-materials coating operations are the surface shear stress components in the radial and azimuthal (tangential) directions, and the heat transfer rate (Nusselt number), which are defined, respectively as:

$$Cf_r = \frac{\mu_{thnf}}{\rho_{thn_f}(r\Omega)^2}\frac{\partial u}{\partial z}\bigg|_{z=0}, \tag{15}$$

$$Cg_r = \frac{\mu_{thnf}}{\rho_{thn_f}(r\Omega)^2}\frac{\partial v}{\partial z}\bigg|_{z=0}, \tag{16}$$

$$Nu = \frac{r}{k_f(T_w - T_\infty)}\left[q_r - k_{thnf}\frac{\partial T}{\partial z}\right]\bigg|_{z=0}, \tag{17}$$

By utilizing equation (9) in Equations (15) – (17), we obtain the dimensionless skin friction components and reduced Nusselt number:

$$Re_r^{1/2} Cf_r = N_1 f''(0) \tag{18}$$

$$Re_r^{1/2} Cg_r = N_1 f'(0) \tag{19}$$

$$Re_r^{-1/2} Nu = -\frac{1}{N_4}(1 + Rd)[1 + \theta(0)(\theta_w - 1)]^3 \theta'(0) \tag{20}$$

Here $Re_r = \frac{\Omega r^2}{\vartheta_f}$ represents *local rotational* Reynolds number.

3. NUMERICAL SOLUTION AND VALIDATION

The final dimensionless governing equations (10) - (12) are highly non-linear. Therefore, it is not possible find exact solutions for these equations. These coupled equations are therefore solved along with relevant boundary constraints numerically by employing a Rung-Kutta fourth/fifth order numerical algorithm with shooting procedure in MATLAB. A Merson modification is also available to accelerate convergence. The following dimensionless parametric values $M = 0.4, \lambda = 0.2, Fr = 0.5, Pr = 6.2, Rd = 1.4, \theta_w = 1.2, \Gamma_t = 0.2, Ec = 0.1$, $\phi_1 = 0.01$, $\phi_2 = 0.02$ and $\phi_3 = 0.03$ are chosen to carry out the numerical calculations for results. This data is extracted from relevant references e.g. [67]-[71] and nanocoating sources [76] to produce physically realistic simulations. In MATLAB this quadrature is used to yield radial velocity function $f'(\zeta)$, azimuthal velocity function $g(\zeta)$ and temperature function $\theta(\zeta)$ in a sub-iteration loop. The stepping formulae are summarized below:

$$k_0 = f(x_i, y_i), \tag{21}$$

$$k_1 = f\left(x_i + \tfrac{1}{4}h, y_i + \tfrac{1}{4}hk_0\right), \tag{22}$$

$$k_2 = f\left(x_i + \tfrac{3}{8}h, y_i + \left(\tfrac{3}{32}k_0 + \tfrac{9}{32}k_1\right)h\right), \tag{23}$$

$$k_3 = f\left(x_i + \tfrac{12}{13}h, y_i + \left(\tfrac{1932}{2197}k_0 - \tfrac{7200}{2197}k_1 + \tfrac{7296}{2197}k_2\right)h\right), \tag{24}$$

$$k_4 = f\left(x_i + h, y_i + \left(\tfrac{439}{216}k_0 - 8k_1 + \tfrac{3860}{513}k_2 - \tfrac{845}{4104}k_3\right)h\right), \tag{25}$$

$$k_5 = f\left(x_i + \tfrac{1}{2}h, y_i + \left(-\tfrac{8}{27}k_0 + 2k_1 - \tfrac{3544}{2565}k_2 + \tfrac{1859}{4101}k_3 - \tfrac{11}{40}k_4\right)h\right), \tag{26}$$

$$y_{i+1} = y_i + \left(\tfrac{25}{216}k_0 + \tfrac{1408}{2565}k_2 + \tfrac{2197}{4101}k_3 - \tfrac{1}{5}k_4\right)h, \tag{27}$$

$$z_{i+1} = z_i + \left(\tfrac{16}{135}k_0 + \tfrac{6656}{12825}k_2 + \tfrac{28561}{56430}k_3 - \tfrac{9}{50}k_4 + \tfrac{2}{55}k_5\right)h. \tag{28}$$

An estimate of the error is achieved by subtracting the two values obtained. If the error exceeds a specified threshold, the results can be re-calculated using a smaller step size. The approach to estimating the new step size is shown below:

$$h_{new} = h_{old}\left(\frac{\varepsilon h_{old}}{2|z_{i+1}-y_{i+1}|}\right)^{\frac{1}{4}}. \tag{29}$$

To assess the accuracy of the employed numerical scheme, a comparison of radial velocity $f'(0)$ and azimuthal velocity gradient $g'(0)$ at the disk surface, for distinct values of magnetic interaction parameter, $M,$ is conducted with the simpler models available in the published works of Rashidi *et al.* [49], Mustafa [68], Acharya *et al.* [69], Waini *et al.* [70] and Shamshuddin *et al.* [67] when $Pr = 6.2$ as shown in **Tables 2 & 3** respectively. These tables confirm very good agreement is achieved between the published literature and present results and confidence in the current numerical methodology is therefore justifiably high.

Table 2: Computational values of $f'(0)$ for distinct values of M when $Pr = 6.2$.

M	Rashidi *et al.* [49]	Mustafa [68]	Acharya *et al.* [69]	Waini *et al.* [70]	Shamshuddin *et al.* [67]	Present results
0	0.510233	0.510186	0.510203	0.510216	0.510214	0.5102136
1	0.309258	0.309242	0.309237	0.309258	0.309258	0.3092564
4	0.162703	0.162701	0.162702	0.162703	0.162703	0.1627012

Table 3: Computational values of $g'(0)$ for distinct values of M when $Pr = 6.2$.

M	Rashidi *et al.* [49]	Mustafa [68]	Acharya *et al.* [69]	Waini *et al.* [70]	Shamshuddin *et al.* [67]	Present results
0	0.61592	0.61589	0.61590	0.61591	0.61592	0.615919
1	1.06905	1.06907	1.06906	1.06905	1.06906	1.069051
4	2.01027	2.01026	2.01027	2.01026	2.01027	2.010274

4. GRAPHICAL RESULTS AND DISCUSSION

The influence of all key parameters on the radial velocity function $f'(\zeta)$, azimuthal velocity function $g(\zeta)$ and temperature function $\theta(\zeta)$ for three different nanofluids i. e. ternary hybrid nanofluid, binary hybrid nanofluid and mono nanofluid are displayed graphically in **Figs. 2-**

15. Also, the impacts of selected parameters on skin friction components and Nusselt number are plotted in **Figs. 16-19** and **Tables 4-6**.

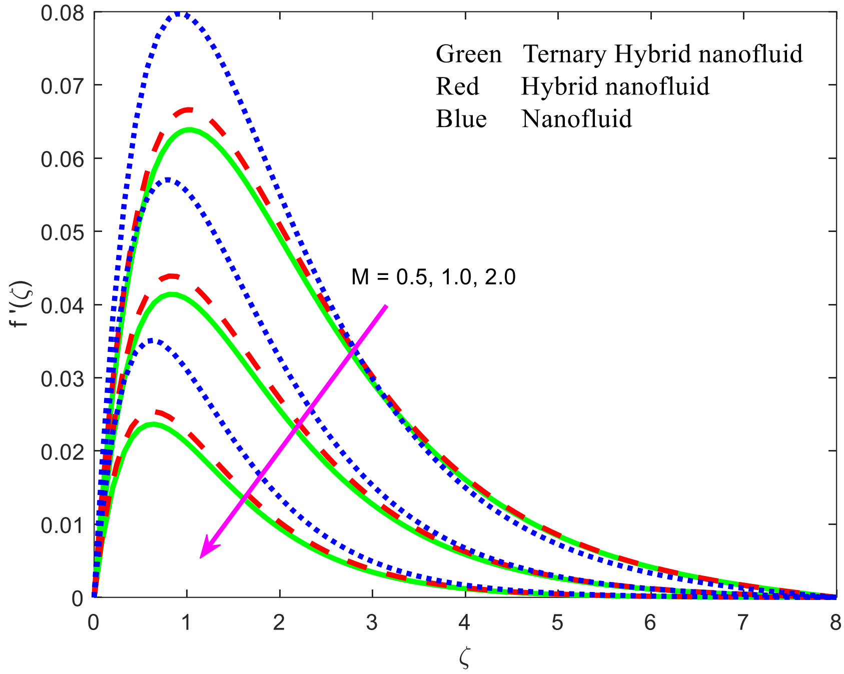

Fig.2. Influence of M on $f'(\zeta)$.

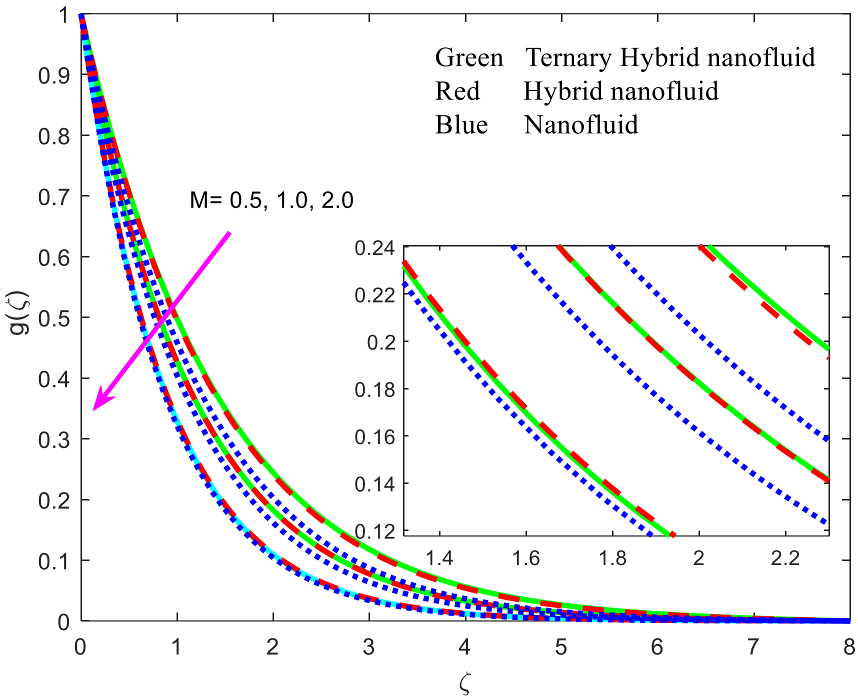

Fig.3. Influence of M on $g(\zeta)$.

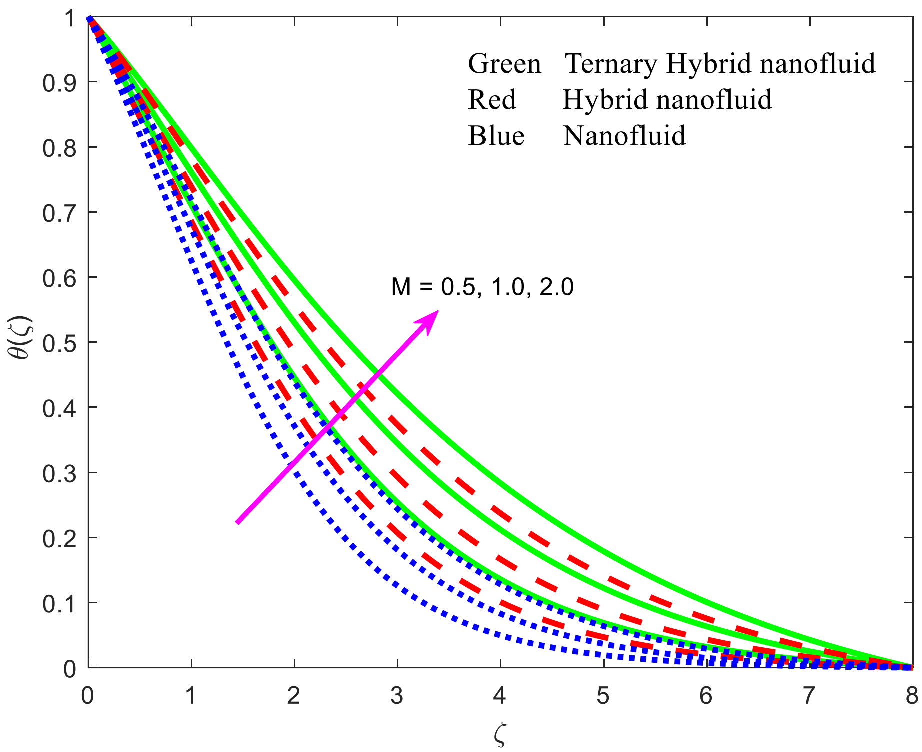

Fig.4. Influence of M on $\theta(\zeta)$.

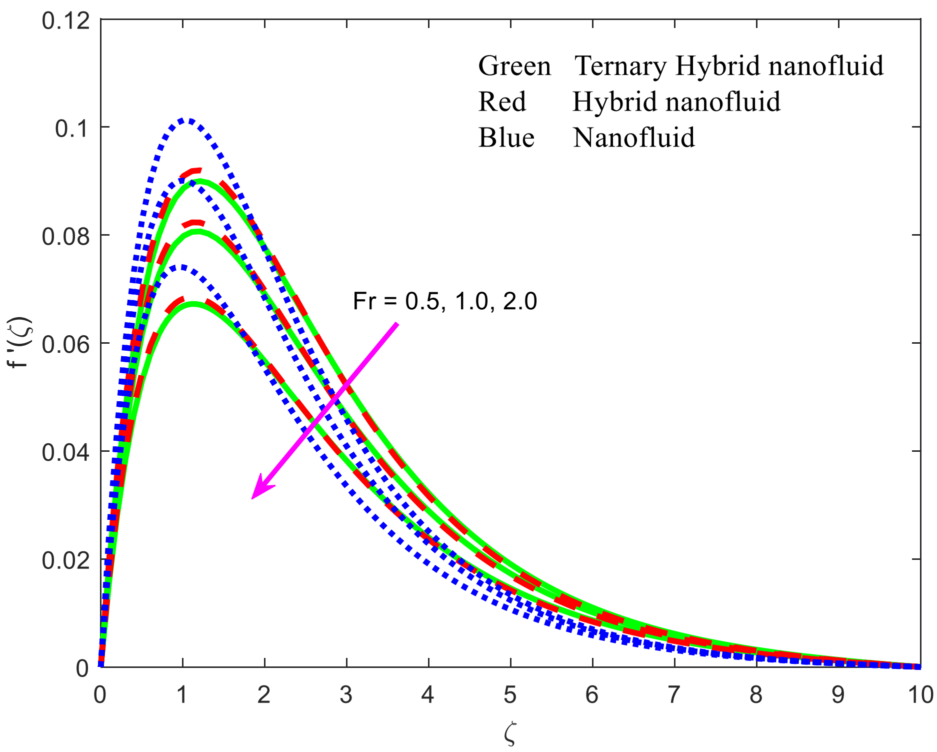

Fig.5. Influence of Fr on $f'(\zeta)$.

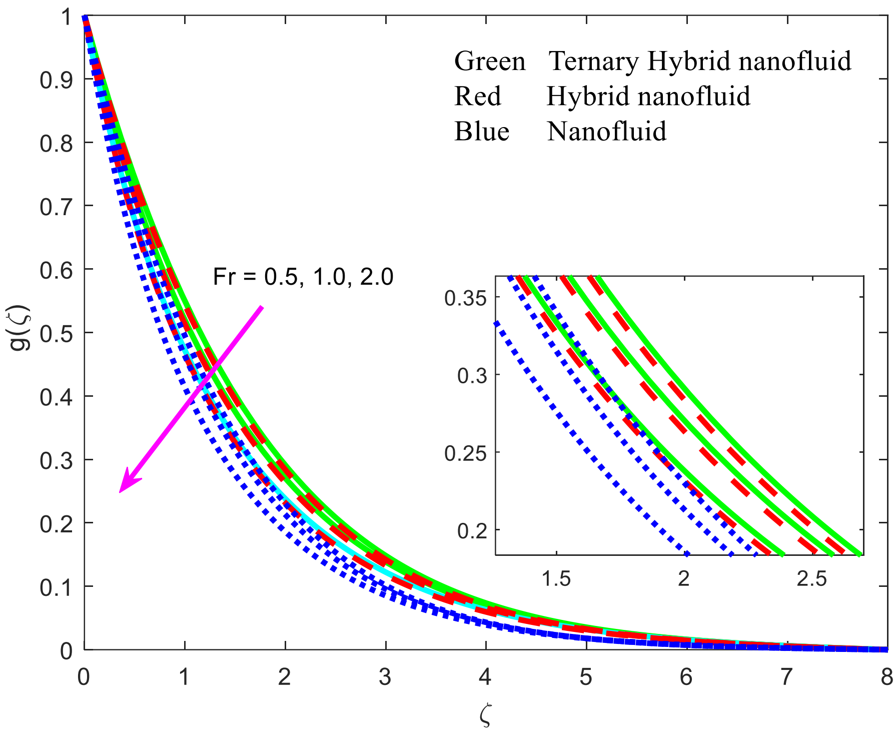

Fig.6. Influence of Fr on $g(\zeta)$.

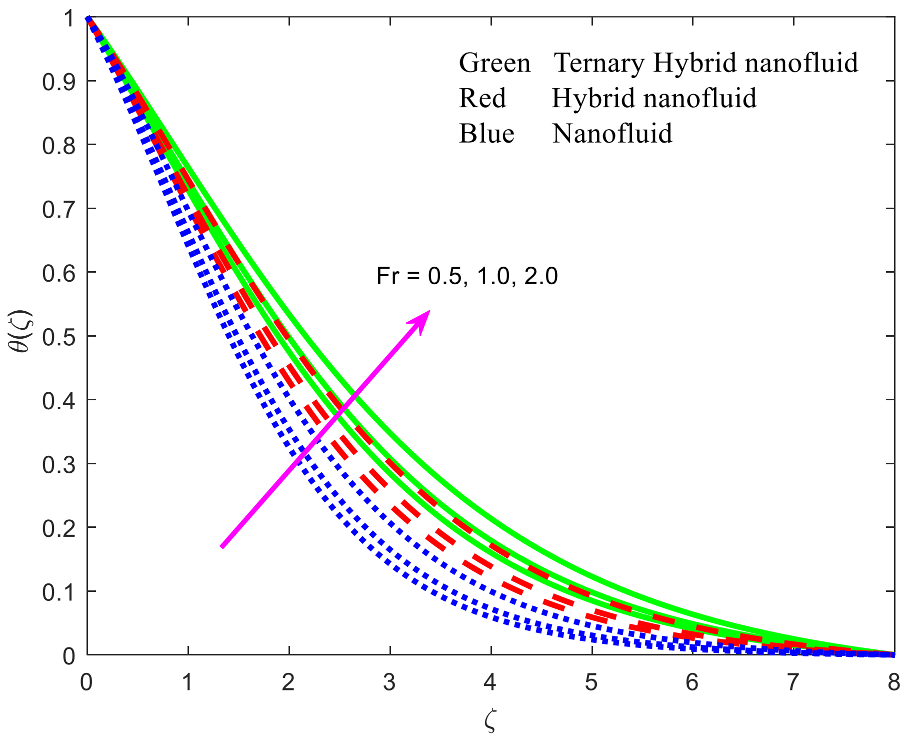

Fig.7. Influence of Fr on $\theta(\zeta)$.

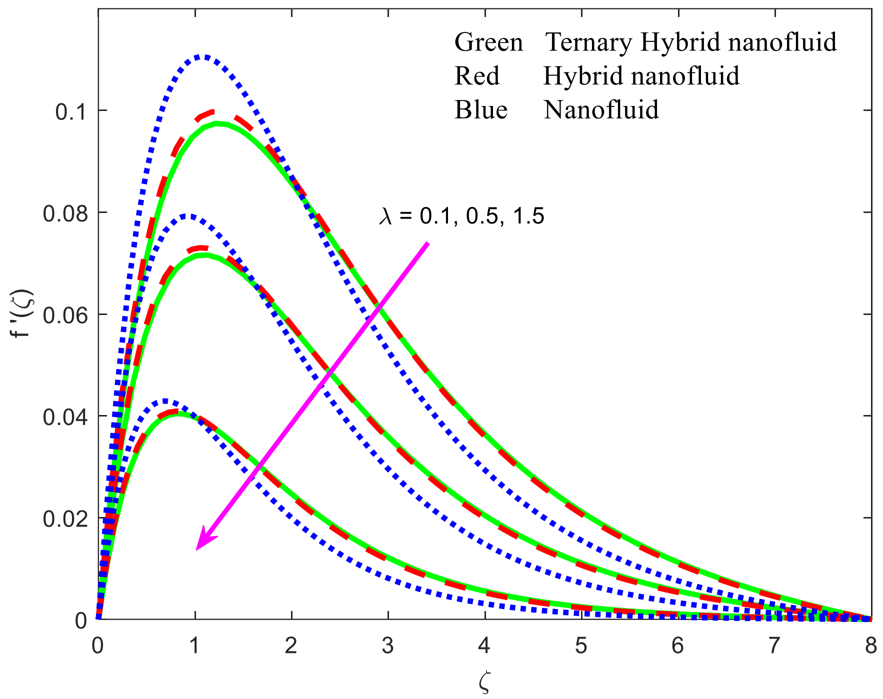

Fig.8. Influence of λ on $f'(\zeta)$.

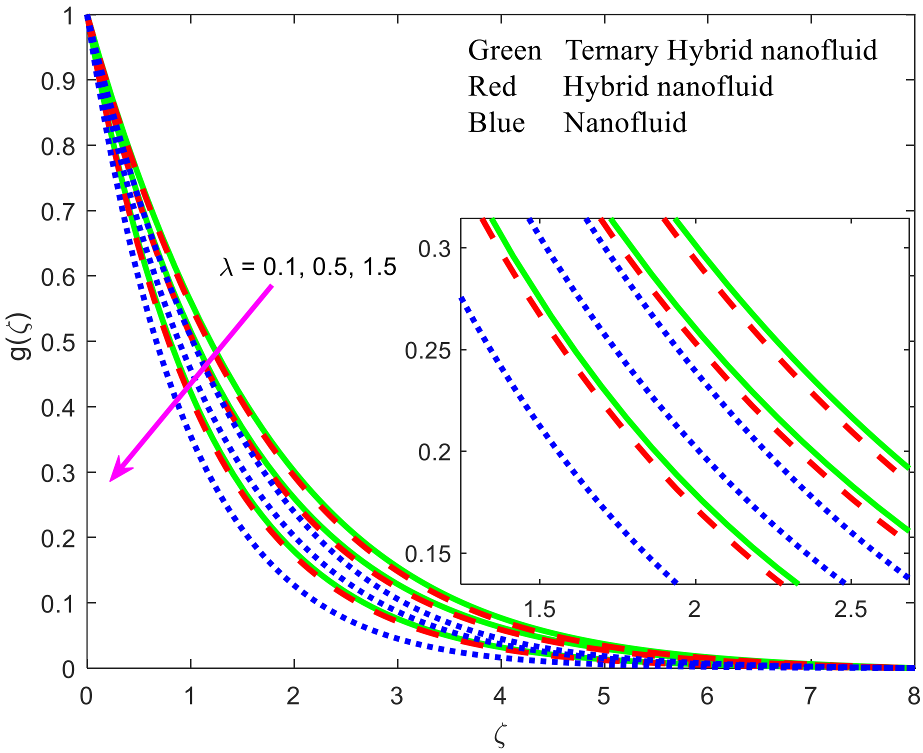

Fig.9. Influence of λ on $g(\zeta)$.

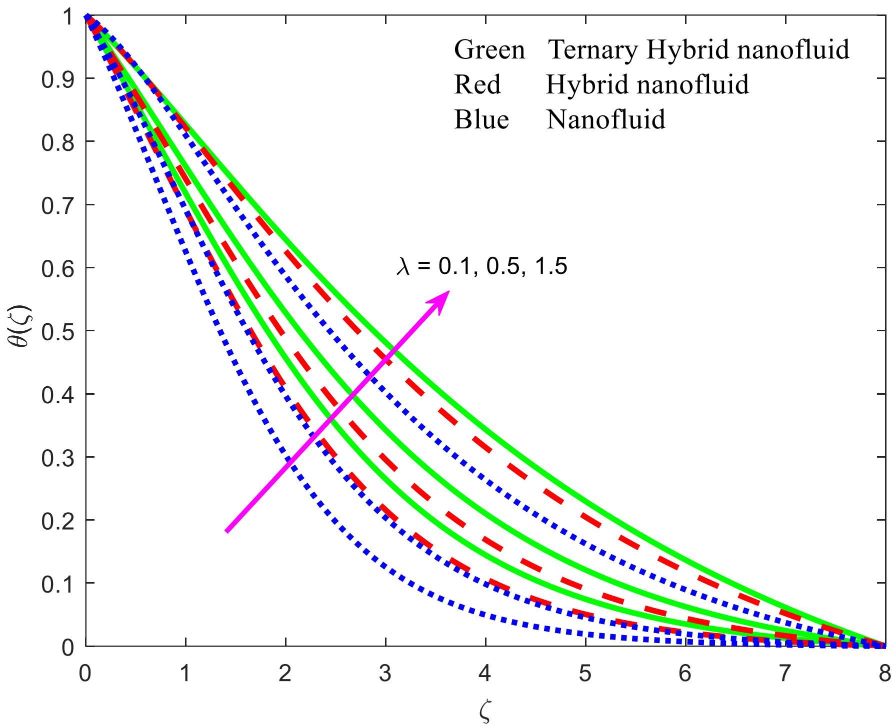

Fig.10. Influence of λ on $\theta(\zeta)$.

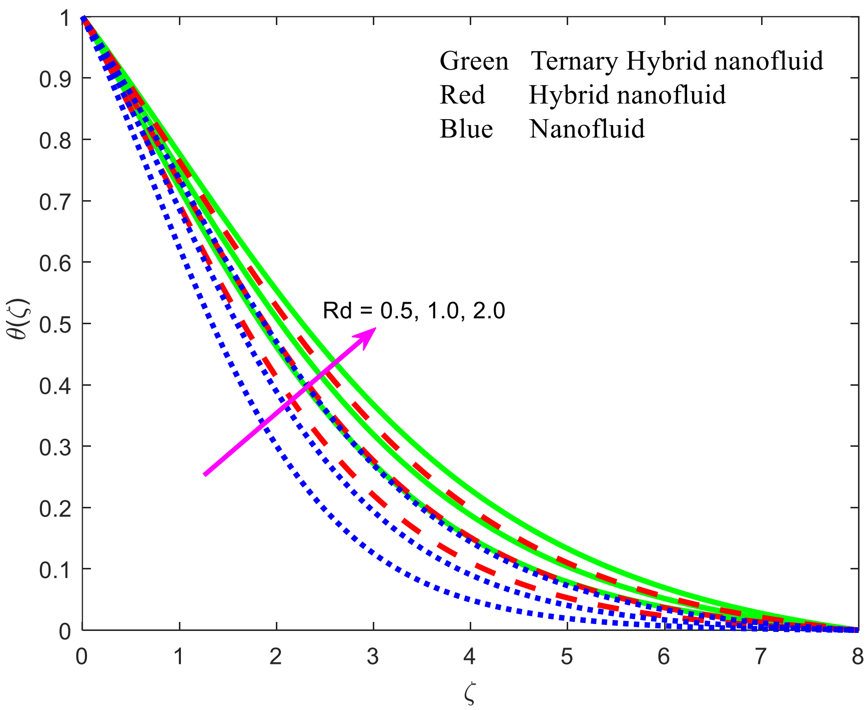

Fig.11. Influence of Rd on $\theta(\zeta)$.

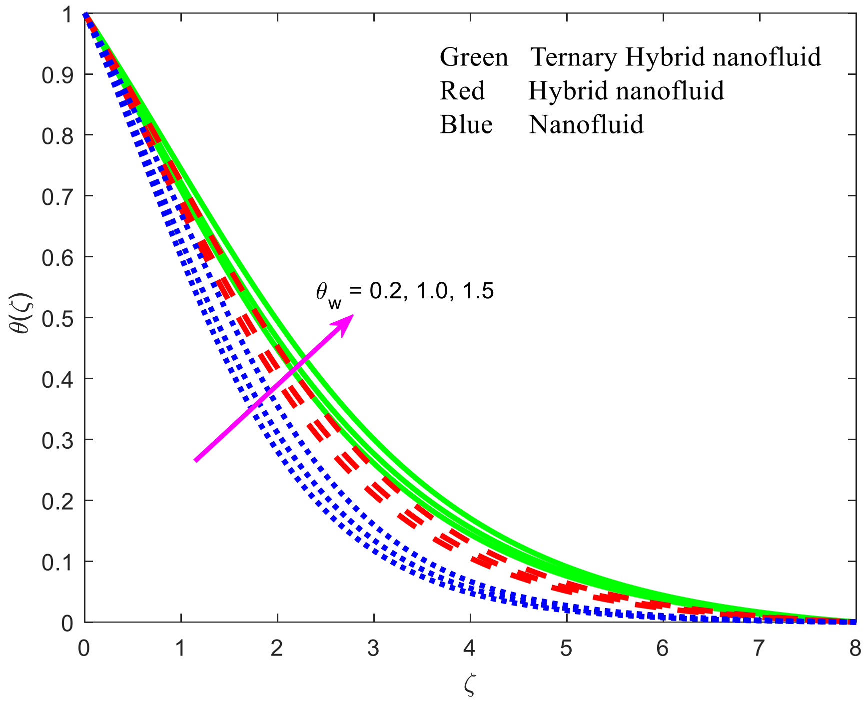

Fig.12. Influence of θ_w on $\theta(\zeta)$.

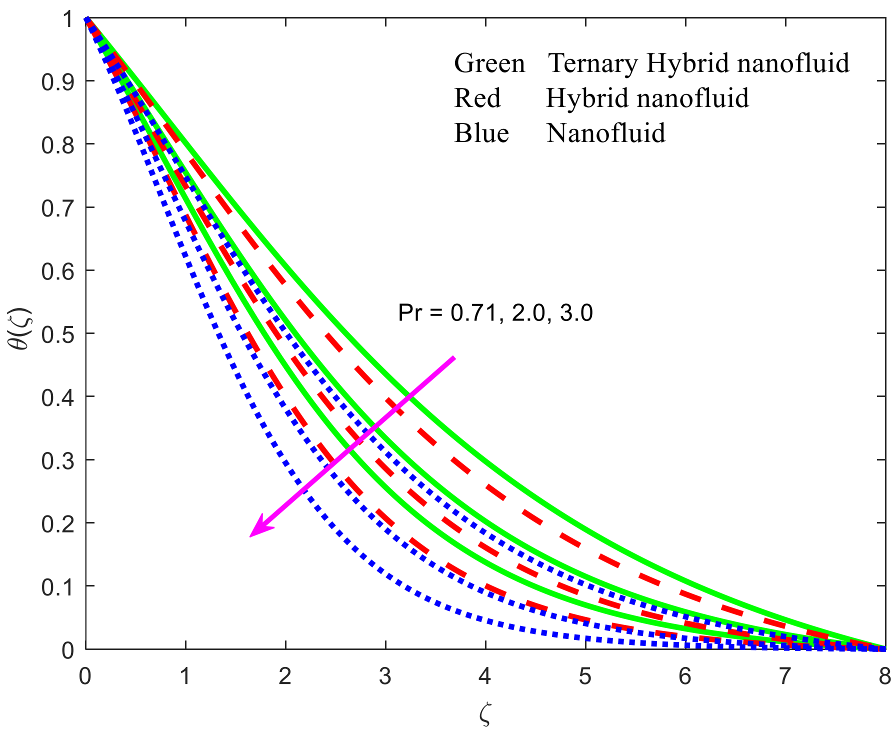

Fig.13. Influence of Pr on $\theta(\zeta)$.

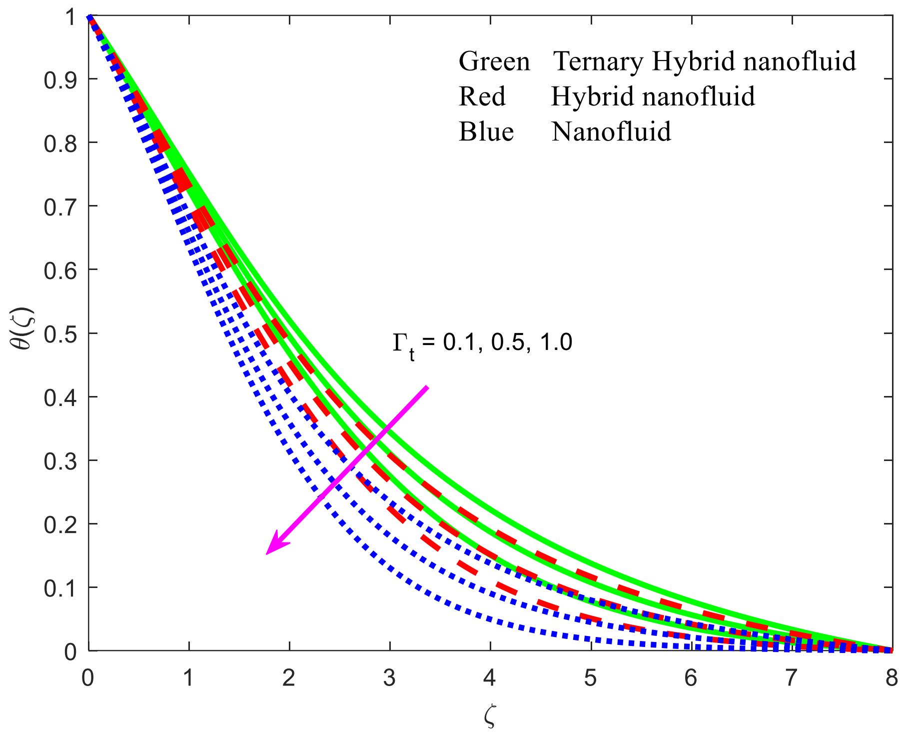

Fig.14. Influence of Γ_t on $\theta(\zeta)$.

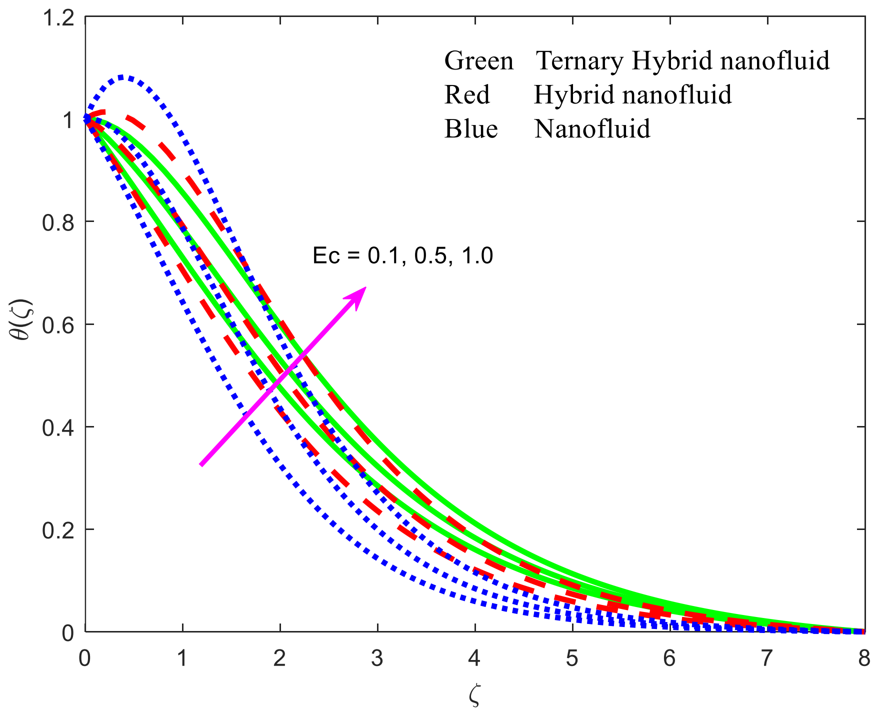

Fig.15. Influence of Ec on $\theta(\zeta)$.

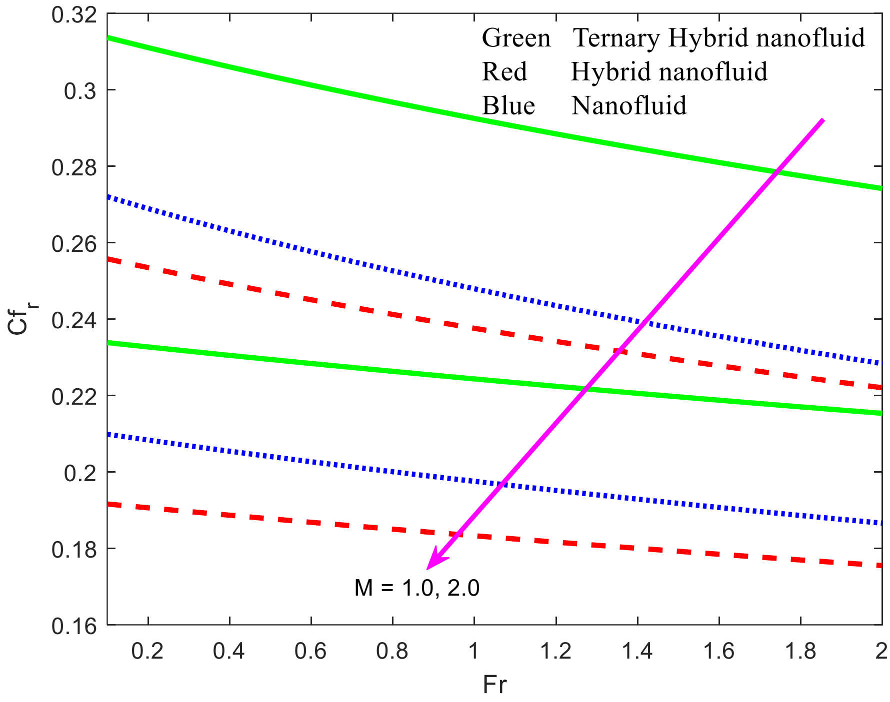

Fig.16. Influence of M and Fr on Cf_r.

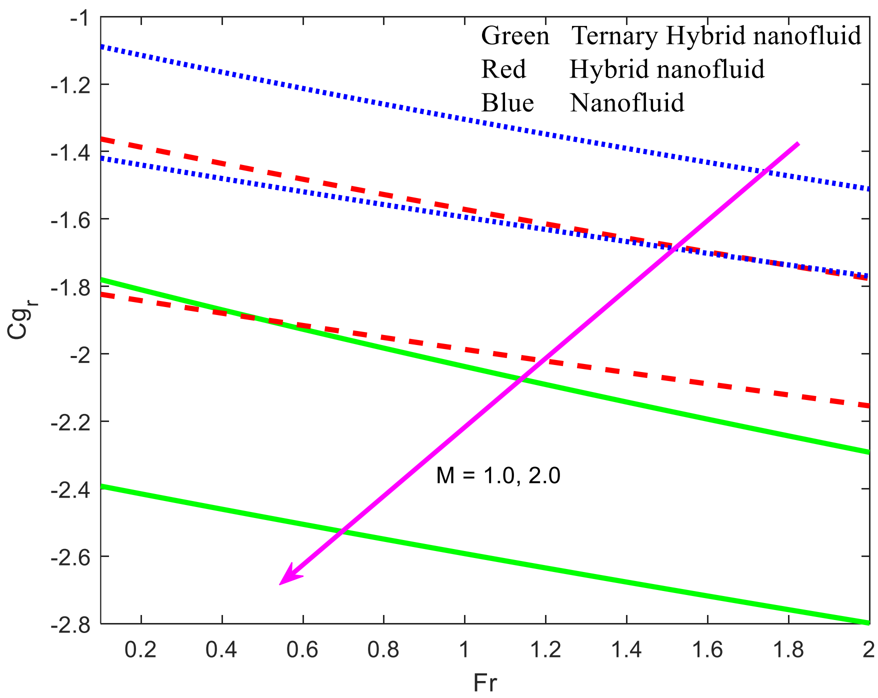

Fig.17. Influence of M and Fr on Cg_r.

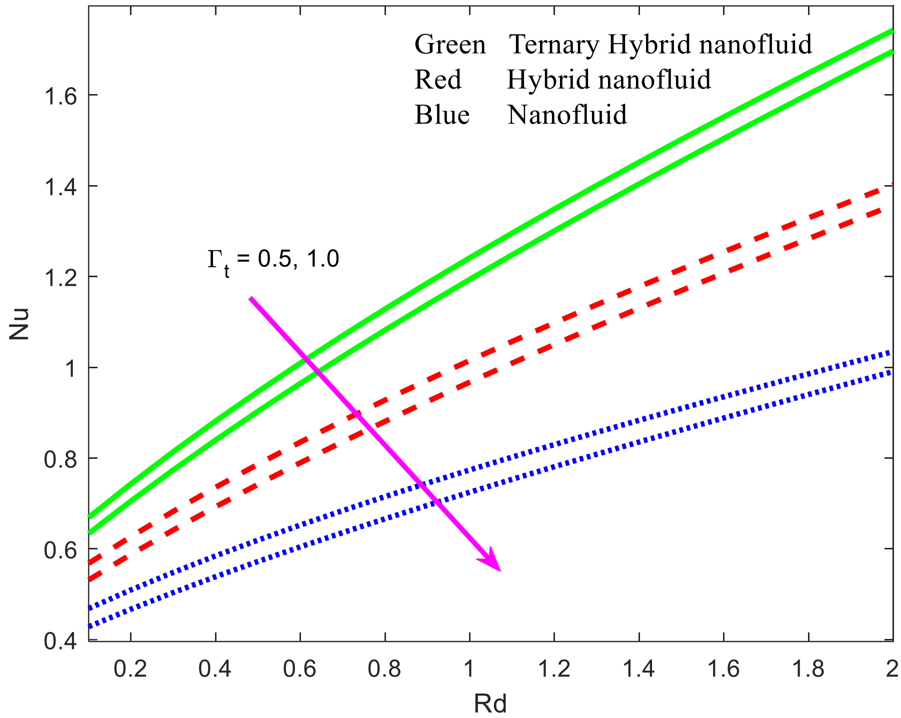

Fig.18. Influence of Γ_t and Rd on Nu.

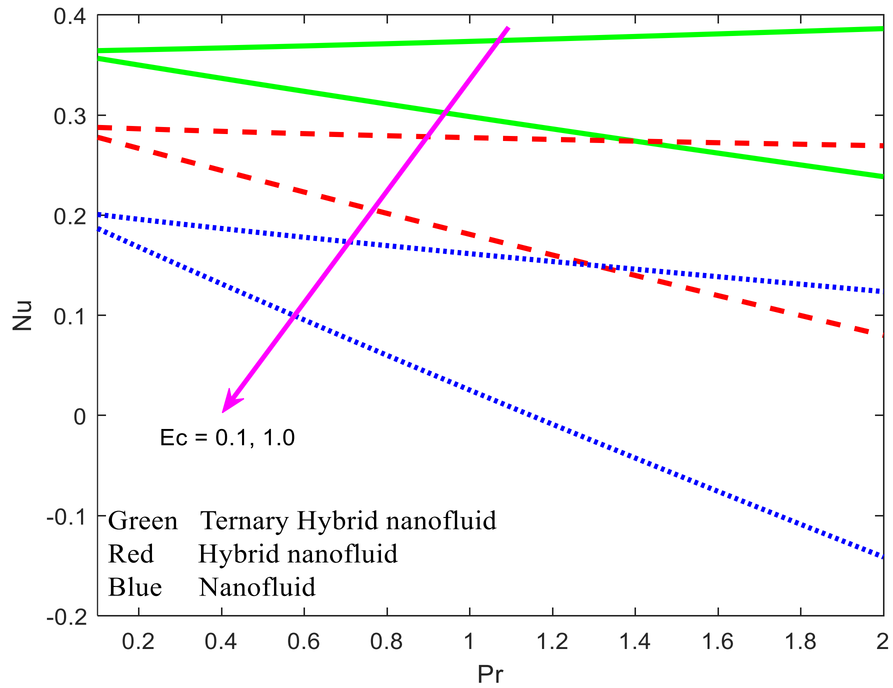

Fig.19. Influence of Ec and Pr on Nu.

Table-4: Numerical results for radial skin-friction (Cf_r) with different values of Fr, λ and M.

Fr	λ	M	Cf_r		
			Tri-Hybrid Nanofluid	Binary Hybrid Nanofluid	Mono-Nanofluid
0.1	0.2	0.5	0.396421	0.320581	0.327250
0.5			0.377922	0.305101	0.308971
1.5			0.342187	0.275392	0.274897
	0.5		0.344114	0.276969	0.276586
	1.0		0.302161	0.242286	0.237814
	1.5		0.271851	0.217414	0.210926
		1.0	0.303571	0.247058	0.260310
		2.0	0.229428	0.187742	0.204032
		3.0	0.191397	0.156917	0.172501

Table-5: Numerical results for azimuthal skin- friction (Cg_r) with different values of Fr, λ and M.

Fr	λ	M	Cg_r		
			Tri-Hybrid Nanofluid	Binary Hybrid Nanofluid	Mono-Nanofluid
0.1	0.2	0.5	1.396486	1.077151	0.893623
0.5			1.540108	1.192701	1.008900
1.5			1.704812	1.324903	1.139374
	0.5		1.684604	1.308475	1.122322
	1.0		1.907051	1.486557	1.296122
	1.5		2.109735	1.648566	1.453079
		1.0	1.898599	1.459163	1.189228
		2.0	2.483253	1.897846	1.499916
		3.0	2.959847	2.257281	1.761874

Table-6: Numerical results for Nusselt number (Nu) with different values of Rd , θ_w, Γ_t, *and* Ec.

Rd	θ_w	Γ_t	Ec	Nu		
				Tri-Hybrid Nanofluid	Binary Hybrid Nanofluid	Mono-Nanofluid
0.1	1.2	0.2	0.1	0.558213	0.471284	0.404657
0.5				0.792700	0.654384	0.535709
1.5				1.045858	0.849044	0.669613
	0.5			0.509073	0.433363	0.379198
	1.5			0.717474	0.593856	0.489219
	2.0			0.934980	0.755426	0.595028
		0.4		0.612452	0.510801	0.427272
		0.6		0.604904	0.501917	0.414873
		0.8		0.597949	0.493756	0.403369
			0.2	0.620661	0.520479	0.440529
			0.3	0.616470	0.515536	0.433799
			0.4	0.612452	0.510801	0.427272

Figs.2-4 elucidate the impact of magnetic interaction parameter, M, on the radial velocity function $f'(\zeta)$, azimuthal velocity function $g(\zeta)$, and temperature function $\theta(\zeta)$ for the three different nanofluids i.e. tri-hybrid Cobalt ferrite ($CoFeO_4$)- Silver (Ag)- Titanium dioxide (TiO_2) $/EGW$ ($C_2H_6O_2$-H_2O 40: 60%)) nanofluid, binary hybrid Cobalt ferrite ($CoFeO_4$) - Silver (Ag) nanofluid and mono Cobalt ferrite ($CoFeO_4$) nanofluid. From Fig. 2, it is evident that the radial fluid velocity is reduced with higher applied magnetic field. The higher magnetic field causes the Lorentzian radial drag component $-\frac{N_3}{N_2}Mf'$ featured in the radial momentum conservation boundary layer eqn. (10) to increase. This impedes the radial momentum and depletes the radial velocity. The peak velocity near the disk surface is also trans-located closer to the disk surface with stronger magnetic field intensity. The parameter $M = \frac{\sigma_f B_0^2}{\rho_f \Omega}$ is a modification of the Stuart magnetic interaction parameter for linear flows to a rotational magnetic interaction parameter. It characterizes the relative role of Lorentzian drag to the

Coriolis body force. When M = 1 both forces contribute equally. For M < 1 the Coriolis force dominates and for M > 1 the Lorentzian magnetic drag force dominates. Under both conditions there will be however significant influence imparted by the magnetic field. The radial flow will be decelerated indicating that the viscous pump action of the rotating disk will be modified. The strong radial deceleration induced allows significant control of the radial flow which in turn influences the distribution of nanoparticles in the coating. This enables considerable manipulation to be achieved in regulating the constitution of nano-coatings during the manufacturing process, as elaborated in Jiang *et al.* [72] since it permits effective use of the out-of-plane magnetic field for nanoparticle assembly. While strong deceleration is induced in the radial field, it is however noteworthy that negative velocities are never incurred. In other words the inhibiting influence of radial Lorentzian magnetic drag never induces flow reversal and flow separation is not observed. Laminar behaviour is sustained. With much higher magnetic field intensity this may arise and therefore judicious selection of the strength of the applied magnetic field is required during spin coating operations as emphasized in [75, 76]. Fig. 2 also shows that radial velocity is much greater for the mono-nanofluid as compared to other hybrid nanofluids. In fact, the ternary hybrid nanofluid exhibits maximum deceleration in the radial flow. This is possibly attributable to the ramping up in viscosity of the nanofluid with the simultaneous presence of three nanoparticles which produces the best flow control during spin coating (note there are nanofluid property constants arising in the radial Lorentzian drag force, viz $N_2 = \frac{\rho_{thnf}}{\rho_f}, N_3 = \frac{\sigma_{thnf}}{\sigma_f}$ which will inevitably contribute). The thickness of the associated hydrodynamic (momentum) boundary layer is therefore increased with stronger magnetic field since momentum diffusion is inhibited. Fig.3 indicates that increment in magnetic field parameter, M, again strongly depletes the azimuthal velocity $g(\zeta)$. This behaviour is sustained as with the radial velocity distribution at all locations into the boundary layer transverse to the disk surface i. e. at all values of ζ. The axial magnetic field, B_o, generates two linear magnetic body force components, which are mutually orthogonal to each other and also perpendicular to the vertical axis. These act in the radial direction and azimuthal direction. The azimuthal Lorentzian drag, $-\frac{N_3}{N_2}Mg$ in eqn. (11), however has a less prominent effect on azimuthal momentum. The radial profiles are inverted parabolas since the radial flow is dominant. The azimuthal distributions are however monotonic decays from the disk surface to the free stream. Stronger magnetic field ramps up the M value which in turn boosts the azimuthal Lorentzian drag and this weakly reduces the azimuthal velocity magnitudes. Again, positive values are maintained throughout the regime indicating an absence of backflow.

Asymptotically smooth profiles are computed at all values of M confirming the prescription of an adequately large infinity boundary condition in the MATLAB solver. Overall, both the radial and azimuthal (tangential) velocity distributions are damped with stronger magnetic field, although the effect is much more significant in the radial field. Dual flow control is therefore achieved via the application of an external static non-intrusive magnetic field, enabling a very powerful mechanism for regulating the coating swirl dynamics. Slightly greater azimuthal velocity $g(\zeta)$ is computed however for the ternary nanofluid and progressively lower magnitudes for the binary hybrid nanofluid and then the mono nanofluid, at weak magnetic field (M = 0.5) although this behaviour is modified at higher M values. Clearly the azimuthal field is influenced differently from the radial field via the presence of nanoparticles and at different magnetic field intensities. From Figs. 2 and 3, it is revealed that the impact of applied magnetic field on dimensionless radial velocity function $f'(\zeta)$ and azimuthal velocity function $g(\zeta)$ produces a similar response. It is observed from Fig.4 that temperature function $\theta(\zeta)$ is escalated with boosting in the applied magnetic field M. Although there is no presence of magnetic field in the energy eqn. (12) since Joule heating (Ohmic dissipation) is neglected, there is however strong coupling with the radial momentum eqn. (10) via the convective term, $+2N_4N_5Prf\theta'$, and the non-Fourier terms, $-Pr\Gamma_t(f^2\theta''+ff'\theta')$. Additionally, the temperature field is coupled to both radial and azimuthal velocity fields via the viscous heating term, $+\frac{N_1}{N_5}\mathrm{Pr}\,Ec[(f'')^2+(g')^2]$. These couplings result in a tangible influence of magnetic field indirectly on the temperature field. As M increases, greater work must be performed to drag the magnetic nanofluid against the action of the magnetic field. This supplementary work is dissipated as heat which elevates temperatures and increases thermal boundary layer thickness. This effect has been reported in numerous studies in the literature including Sparrow and Cess [15] for viscous fluids and Shahzad *et al.* [65] for magnetic ternary nanofluids. This effect is sometimes referred to as the magnetocaloric effect (MCE) and Is characterized by either heating or cooling of a magnetic material with modification in applied magnetic field intensity. At weak magnetic field values (M = 0.5) the temperature profiles exhibit a strongly parabolic topology. However, this becomes essentially linear at higher M values, for example at M = 2 where the Lorentzian body force components are double the Coriolis force. Significantly greater temperature is computed for the ternary hybrid nanofluid ($CoFeO_4$-Ag-TiO_2/EGW) as contrasted to other two nanofluids, at all values of M and all locations in the boundary layer. This confirms the substantial thermal enhancement achieved with doping the base fluid with three nanoparticle types which act in unison to ramp up thermal conductivity and therefore encourage heat diffusion through the boundary layer. The thermal boundary layer thickness is therefore maximum for the ternary hybrid nanofluid ($CoFeO_4$-Ag-TiO_2/EGW), lower for the hybrid binary $CoFeO_4$-Ag nanofluid and minimal for the $CoFeO_4$ unitary nanofluid. Again, smooth convergence of all profiles in the free stream (edge of the boundary layer) is achieved confirming that the infinity boundary condition utilized in the MATLAB code is sufficiently large. Overall, stronger magnetic field is found to markedly damp both the radial $f'(\zeta)$ and azimuthal $g(\zeta)$ flow whereas it considerably enhances temperature $\theta(\zeta)$.

Figs.5-7 illustrate the influence of the Forchheimer quadratic porous drag inertia coefficient Fr on velocity distributions and temperature profiles. A strong reduction in radial velocity is computed with increasing Fr values, for all three nanofluids as observed in Fig.5. In the radial momentum eqn. (10) the linear Darcian drag and second order Forchheimer body forces are defined by the terms, $-\lambda f'$ and $-(1+Fr)f'^2$, respectively. Both are negative since both forces are associated with drag. While the Darcian drag is dominant at lower Reynolds numbers, the Forchheimer drag dominates at higher Reynolds numbers. At Reynolds number of approximately 10, the nonlinear drag effect is invoked, and this is associated with the growth of *microscopic viscous forces* at higher flow velocities. It is important to note that at the onset of nonlinear flow, inertial forces are still several orders of magnitude smaller than interfacial drag forces. Therefore, inertial forces alone do not contribute to the onset of nonlinear flow in porous media. At Reynolds numbers as high as 100, where laminar flow is still present, inertial forces can however become as important as drag forces. With higher Fr values, since the inertial drag is increased the net effect is deceleration of the radial flow. A significant displacement in radial velocity peak towards the disk surface is also induced with increasing Forchheimer parameter. Significant damping of the radial flow is achieved indicating that the presence of solid matrix fibers at higher Reynolds numbers dominates the percolation of the magnetic nanofluid in the porous medium. A significant flow control mechanism is therefore also available via inertial drag. In the present analysis, the medium is simplified to ignore tortuosity (intertwining of paths between pores) and anisotropy (different permeabilities in different directions). However, these aspects could conceivably also contribute to the inertial drag effect and may be examined in future studies. In fig. 5 despite the strong deceleration effect induced with higher inertia coefficient Fr there is no reversal in radial flow computed. At further distances from the disk surface, the ternary nanofluid and binary nanofluid achieve approximately the same magnitudes of radial velocity which exceeds that of the unitary nanofluid. Closer to the disk surface, this trend is altered. The unitary nanofluid attains the highest velocities in the near-wall region, followed by the binary hybrid nanofluid and the lowest radial velocity is observed for the ternary hybrid nanofluid. The response in radial velocity for each nanofluid is therefore *dependent on the location in the boundary layer* and this may be attributable to the clustering effect of multiple nanoparticles closer to the disk surface which induces deceleration. This effect is not prevalent further from the wall. Fig. 6 shows that the azimuthal velocity $g(\zeta)$ is also reduced with higher values of Fr. The modification is however less dramatic than for the radial (primary) flow since the azimuthal field is the secondary flow field in the swirling regime. As with the radial velocity field, there is also a Forchheimer drag component present in the azimuthal momentum eqn. (11), $-Frg^2$. Increasing Fr will clearly boost this retarding force. The effect will be increasingly pronounced at higher magnitudes of azimuthal velocity $g(\zeta)$. Therefore, while the nanofluids may appear to be exhibiting higher velocity, the porous inertial drag will dominate and in fact retard the flow more significantly. The nonlinear dependence of interfacial drag forces on the azimuthal flow velocity will decelerate the flow. The inertial drag has also been shown to be strongly dependent on the constitution of the porous medium i. e. the nature of the solid fibres which naturally vary from one material to another. Coating designers can therefore exercise some control in selecting appropriate porous materials for the filtration damping mechanism. Contrary to the radial velocity distribution relationship with nanofluid type, maximum azimuthal velocity is always computed for the ternary ($CoFeO_4$-Ag-TiO_2/EGW) hybrid nanofluid and is marginally greater than the binary hybrid nanofluid, but much larger than the unitary $CoFeO_4$ nanofluid, at all values of axial coordinate (ζ). The three different nanofluids therefore produce a very different effect on the radial and azimuthal momentum distributions. The implication is that designers must be aware of the complex variations in behaviour produced with different nanoparticle doping in the different velocity fields and carefully select different nanoparticle combinations to achieve desired outputs in coatings. Fig. 7, illustrates that the nanofluid temperature consistently increases with larger inertia coefficient parameter Fr. In addition, the Cobalt ferrite unitary nanofluid temperature is lowest and the ternary hybrid nanofluid is the highest, confirming the significant boost in thermal conductivity achieved with tri-hybrid nanoparticles which heats the boundary layer regime significantly. The damping in the radial and azimuthal momentum implies that momentum diffusion is swamped by thermal diffusion (since Prandtl number is prescribed as 6.2). This encourages more efficient thermal convection in the magnetic nanofluid which elevates temperatures. A homogenous distribution in temperature is achieved from the disk surface to the free stream.

Figs.8-10 illustrate the impact of inverse permeability parameter λ on radial velocity $f'(\zeta)$, azimuthal velocity field $g(\zeta)$ and temperature field $\theta(\zeta)$. This parameter features in both the radial and azimuthal momenta equations (10, 11) in the linear terms, $-\lambda f'$ and $-\lambda g$. Since $\lambda = \frac{\vartheta_f}{\Omega K^*}$, these Darcian drag force terms are inversely proportional to the permeability of the porous medium K^*, for a given value of disk spin velocity (Ω) and base fluid kinematic viscosity ϑ_f. As the inverse permeability parameter λ is elevated, the permeability of the porous medium is decreased and the Darcian drag components are hiked. This produces a boost in solid matrix fiber resistance to the percolating nanofluid and strongly reduces both radial and tangential velocity components. Strong damping can therefore be easily generated in the coating swirling regime via the prescription of more tightly packed porous media which again provides materials engineers with another excellent mechanism for flow regulation. With progressive increase in Darcian parameter the peak radial velocity (Fig. 8) is shifted nearer the disk surface (ζ=0) and furthermore the three nanofluids exhibit different behaviours. Closer to the wall ternary hybrid nanofluid corresponds to maximum radial deceleration and unitary nanofluid is associated with maximum radial acceleration. Further from the disk surface both ternary and binary hybrid nanofluids achieve the same radial acceleration whereas strong retardation is exhibited by the unitary nanofluid. This pattern is sustained into the free stream (ζ= 8). The spatial dependence of the different nanofluids is therefore again observed. For the azimuthal velocity (Fig. 9) we observe that marginally greater magnitudes are computed for the ternary hybrid nanofluid followed by slightly lower values for the binary hybrid nanofluid and minimal values for the unitary nanofluid. This trend is maintained at all locations in the boundary layer transverse to the disk surface. Flow reversal is never computed in either velocity field at any value of Darcian inverse permeability parameter, λ. Increasing λ however produces a strong increment in temperature in the regime (Fig. 10). Since the permeability is decreased with greater values of λ, there is a greater concentration of solid fibers in the porous matrix. This encourages thermal conduction which contributes to the boost in temperatures and results in a thicker thermal boundary layer on the disk surface. Again, temperature is highest for tri-hybrid nanofluid $CoFeO_4$-Ag-TiO_2 and lowest for unitary nanofluid $CoFeO_4$ with the binary hybrid nanofluid intercalated between the other two cases on all temperature plots. Substantial heating can be induced in the swirling regime therefore with the deployment of ternary hybrid nanofluid in conjunction with a low permeability filtration material.

Fig.11. displays the impact of thermal radiation parameter Rd on non-dimensional temperature $\theta(\zeta)$ for all three nanofluids. The numerical results show that nanofluid temperature escalates

as the values of Rd increase. $Rd = \frac{16\sigma^* T_\infty^3}{3k^* k_f}$ and is present in the augmented thermal diffusion terms in the energy Eqn. (12), $+RdN_4 \frac{d}{d\zeta}\left([1 + \theta(\zeta)(\theta_w - 1)]^3 \theta'(\zeta)\right)$. This parameter represents the relative contribution of thermal radiation to thermal conduction in the regime. When *Rd = 0* radiative flux vanishes (infinite thermal conduction contribution). When *Rd* > 0 thermal radiation is present. For *Rd =1* both thermal radiative and thermal conduction modes contribute equally. For *Rd* > *1* thermal radiation dominates. Clearly the boost in radiative flux energizes the regime. This produces a hike in temperature and a greater thermal boundary layer thickness. Similar observations have been reported in for example [61] and [63]. Also, the temperature of $CoFeO_4$ unitary nanofluid is the least; higher temperature is produced with binary hybrid nanofluid, and the maximum corresponds to tri-hybrid $CoFeO_4$-Ag-TiO_2 nanofluid. It is also noticed that the thermal boundary layer thickness is enhanced with a boost in thermal radiation which is consistent with the optically thick Rosseland approximation.

Fig.12 illustrates the behaviour of nanofluid temperature $\theta(\zeta)$ for all three nanofluids with temperature ratio parameter θ_w. $\theta_w = \frac{T_w}{T_\infty}$. When θ_w > 1, the wall (disk surface) temperature exceeds the free stream temperature. When θ_w < 1 the opposite scenario arises and the wall temperature is exceeded by the free stream temperature. Increment in the temperature ratio clearly strongly elevates temperature at all locations in the boundary layer. Thermal conduction from the hotter disk to the ambient nanofluid is encouraged especially when θ_w > 1 due to the assistive temperature difference. It is found that thermal boundary layer thickness is therefore boosted with higher temperature ratio parameter θ_w. Again, there is a substantially greater temperature achieved for the ternary nanofluid relative to the hybrid nanofluid and unitary nanofluid. This behaviour is consistent throughout the boundary layer. The remarkable thermal enhancement properties of tri-hybrid nanofluid are clearly demonstrated.

Fig.13 visualizes the influence of Prandtl number Pron temperature distribution $\theta(\zeta)$. Pr defines the ratio of momentum and thermal diffusion rates. It is also inversely proportional to thermal conductivity for a given dynamic viscosity and specific heat capacity. When *Pr = 1* both momentum and thermal diffusion rates are the same and the hydrodynamic and thermal boundary layer thicknesses are also equivalent. For Pr < 1 thermal diffusivity exceeds momentum diffusivity and vice versa for Pr >1. However, the dominant influence is the thermal conductivity. It is much higher when Pr > 1 than when Pr < 1. This results in a strong curtailing in thermal conduction with increment in Prandtl number and depletes temperatures in the nanofluid regime. Thermal boundary layer thickness will also be reduced. Approximately linear decay for the wall (disk surface) accompanies higher *Pr* values whereas a monotonic decay is present for $Pr < 1$. Ternary hybrid nanofluid again produces the greatest heating effect (temperature) whereas unitary nanofluid is associated with the strongest cooling effect (lowest temperature magnitude).

Fig.14 depicts the evolution in temperature distribution with increasing values of non-Fourier thermal relaxation variable Γ_t . A strong depletion is computed in temperature with greater thermal relaxation parameter, Γ_t. The non-Fourier effect introduces a delay in the thermal conduction mechanism. The physical reason for this is that fluid particles take time to pass transfer thermal energy to the neighbouring particles with larger thermal relaxation time (Γ_t) which induces a cooling effect and reduction in temperature. Heat transmission is slowed down from the disk surface to the wall with the hyperbolic model. Thermal boundary layer thickness is also reduced considerably. The Cattaneo-Christov thermal relaxation parameter, $\Gamma_t = \varepsilon_t\Omega$ arises in the augmented diffusion terms, $-Pr\Gamma_t(f^2\theta'' + ff'\theta')$ in Eqn. (12). When $\Gamma_t \rightarrow 0$ thermal relaxation vanishes and the model retracts to the classical Fourier parabolic heat conduction model. This will clearly overpredict temperatures since the heat conduction in this model occurs via diffusion processes, not finite thermal waves as with the non-Fourier model. A more realistic appraisal of actual thermal distribution in the rotating disk flow regime is only possible with the non-Fourier model, in particular, when rapid hot spot loading is used during fabrication processes. The trends computed concur with previous studies for viscous fluids (see Mishra *et al.* [40]) and also other complex coating fluids [39]. As in other plots, maximum temperature enhancement is obtained with the ternary hybrid nanofluid, and the minimum temperatures are produced for unitary nanofluid. The influence of non-Fourier relaxation time is significant and should therefore be incorporated in robust models for nano-coating spin processes.

Fig. 15 displays the influence of Eckert number Ec on the temperature function $\theta(\zeta)$ versus transverse coordinate (ζ). It is note that the temperature is considerably elevated with a rise in Ec values. A temperature overshoot is computed near the disk surface only for the unitary nanofluid for $Ec = 1$ but is absent in all other profiles. Near the disk surface higher temperatures are produced for unitary nanofluid, then for binary hybrid nanofluid and the lowest temperatures are observed for ternary hybrid nanofluid. However further from the wall (disk surface), there is a gradual modification in this behaviour. Eventually ternary nanofluid exhibits the highest temperature with unitary nanofluid producing the lowest temperature. The binary hybrid nanofluid performs better than the unitary nanofluid but does not attain temperatures as high as the hybrid nanofluid, a trend which continues into the free stream. The Eckert number quantifies the effect of viscous heating in the boundary layer. $Ec = \frac{r^2\Omega^2}{T_w}$ and features in the dissipation term, $+\frac{N_1}{N_5}\Pr Ec[(f'')^2 + (g')^2]$. Ec can be regarded as the ratio of rotational kinetic energy in the swirling flow to the boundary layer enthalpy difference. As Ec increases a greater percentage of mechanical energy is converted to thermal energy via the dissipation between nanofluid molecules. This heats the regime and boosts thermal boundary layer thickness. Clearly when viscous heating is neglected, temperatures are under-predicted. This can lead to undesirable results in coating thermal management [74].

The profiles for radial and tangential (azimuthal) skin friction and also Nusselt number for all three nanofluids and selected control parameters is displayed in **Figs. 16-19** respectively. Fig.16 exhibits the change of behaviour of radial skin friction Cf_r for various M and Fr. It is evident that Cf_r is reduced for higher magnetic field and Fr i.e. flow deceleration is induced with greater applied axial magnetic field and inertial drag resistance. It is pertinent to highlight that radial skin friction is minimized for the dual hybrid nanofluid $CoFeO_4$- Ag while it is maximized for the ternary hybrid nanofluid. The unitary nanofluid achieves intermediate radial skin friction magnitudes. Fig.17 indicates that that, the azimuthal friction coefficient Cg_r is also reduced with both an increment in Forchheimer inertia coefficient Fr and magnetic interaction parameter, M. However much higher magnitudes are computed compared with the radial skin friction. Cg_r is markedly greater however for the unitary nanofluid and is minimized for the ternary hybrid nanofluid. The variation in Nusselt number with thermal relaxation variable Γ_t and radiation parameter Rd is plotted in Fig.18. Nusselt number is significantly enhanced with higher thermal radiation Rd whereas the opposite behaviour i. e. a strong depletion in Nusselt number is computed with an increment in Γ_t . Substantially greater magnitudes of Nu are observed at all values of Rd for the ternary hybrid nanofluid; the next highest magnitudes are for the binary hybrid nanofluid and the lowest Nusselt numbers are computed for the unitary nanofluid. The relative contribution of thermal convection to thermal conduction at the disk surface is therefore suppressed most dramatically for the unitary nanofluid. It is concluded from Fig. 19 that the Nusselt number is greatly suppressed with increment in Eckert number, Ec and also depleted with increment in Prandtl number. Since the rotating boundary layer is heated significantly with stronger viscous dissipation, heat is removed from the disk surface and the net heat transfer to the disk surface is depleted. At all values of Ec and up to *Pr ~ 1.4*, ternary hybrid nanofluid sustains the highest Nusselt numbers, followed by binary hybrid nanofluid and then unitary nanofluid. However, for Pr > 1.4, there is a slight cross-over in Nusselt number magnitudes, although generally the ternary nanofluid achieves the best values.

Finally, numerical values computed for radial and tangential skin friction coefficients Cf_r , Cg_r and Nusselt number Nu for different control parameters and all three nanofluids are presented in **Tables 4-6** respectively. These supplementary solutions also provide a good benchmark reference for future investigations and other researchers to validate the current computations with alternative numerical methods. It is evident from Table 4, that the radial skin-friction coefficient Cf_r is reduced for all three nanofluids with a boost in Forchheimer inertia coefficient Fr , magnetic interaction parameter M and Darcian inverse permeability parameter λ . Binary hybrid $CoFeO_4$-Ag nanofluid exhibits lower values of Cf_r in comparison with ternary nanofluid. Azimuthal skin-friction Cg_r is observed to be elevated with inertia coefficient Fr , magnetic interaction parameter M and Darcian inverse permeability parameter λ ., for all three nanofluids in Table-5. The trihybrid $CoFeO_4$-Ag-TiO_2nanofluid produces highest tangential skin friction values in comparison to the other nanofluids. Table-6 shows Nusselt number is markedly boosted with Stark number (radiation-conduction parameter), Rd and temperature ratio, θ_w; however, the opposite trend is observed for greater values of non-Fourier thermal relaxation parameter, Γ_t and Eckert number, Ec. Furthermore, the ternary nanofluid clearly attains the best Nusselt number magnitudes and achieves the *greatest heat transfer rate to the disk surface* relative to the other two nanofluids.

5. CONCLUSIONS

As a simulation of smart magnetic nano-material spin coating manufacturing, a theoretical analysis of Von Karman swirl flow of magnetic ternary hybrid nanofluid from a rotating disk under axial constant magnetic field to a non-Darcy isotropic porous medium has been presented. Thermal radiative heat transfer is included via the Rossleand diffusion flux model, thermal relaxation is modelled with a non-Fourier Cattaneo-Christov model and viscous dissipation is also incorporated. $CoFeO_2$-Ag-TiO_2 hybrid nanoparticles are considered with Ethylene Glycol-Water ($C_2H_6O_2 - H_2O$ $40:60\%$) base fluid. The Darcy-Forchheimer drag force model is deployed to simulate both bulk matrix porous drag and inertial quadratic drag. The governing conservation equations for mass, momenta (radial, tangential and axial) and energy with prescribed boundary conditions are transformed into coupled nonlinear ordinary differential boundary layer equations via suitable scaling variables and the Von Karman transformations. The derived reduced boundary value problem is then solved with a Runge-Kutta numerical scheme and shooting scheme in MATLAB. Validation of solutions is included with previous studies demonstrating exceptional accuracy. Radial and azimuthal velocities, temperature, radial skin-friction, azimuthal skin friction and local Nusselt number are computed for a range of selected parameters. A comparative assessment of mono nanofluid $CoFeO_2$, Hybrid $CoFeO_2$-Ag nanofluid and tri- Hybrid $CoFeO_2$-Ag-TiO_2 nanofluid is conducted. The principal findings of the present study can be crystallized as follows:

1) Radial and tangential (azimuthal) flows are both decelerated (and the associated hydrodynamic boundary layer thickness is increased) with an increase in magnetic interaction parameter whereas temperature and thermal boundary layer thickness are both increased.
2) Radial and tangential (azimuthal) flows are both retarded with an increment in Forchheimer inertial parameter and Darcy inverse permeability parameter whereas temperature is elevated with both these parameters.
3) Temperature is suppressed with increasing Prandtl number and non-Fourier thermal relaxation parameter whereas it is boosted with an increment in temperature ratio parameter, Eckert number and radiation-conduction parameter (Stark number).
4) Radial velocity is greater for the unitary $CoFeO_4$ nanofluid as contrasted to other two hybrid nanofluids $CoFeO_4$-Ag-TiO_2/EGW and $CoFeO_4$-Ag/EGW.
5) A strong depletion is perceived in temperature and thermal boundary layer thickness is computed with greater thermal relaxation parameter, Γ_t indicating that the hyperbolic heat conduction produces a cooling effect relative to the classical parabolic (Fourier) model.
6) The radial skin friction is reduced for higher magnetic field and Forchheimer parameter.
7) Azimuthal friction is depleted with both an increment in Forchheimer inertia coefficient and magnetic interaction parameter, but significantly greater magnitudes are observed compared with the radial skin friction.
8) Radial skin friction is least for the dual hybrid nanofluid $CoFeO_4$- Ag while it is greatest for the ternary hybrid nanofluid. Azimuthal skin friction is however a maximum for the unitary nanofluid and is a minimum for ternary hybrid nanofluid.
9) With increasing thermal radiation parameter, temperature of $CoFeO_4$ unitary nanofluid is smallest whereas it is highest for the tri-hybrid $CoFeO_4$-Ag-TiO_2 nanofluid.

10) The Nusselt number Nu is boosted with radiation parameter and temperature ratio whereas it is strongly reduced with thermal relaxation parameter and Eckert number.
11) Generally ternary hybrid $CoFeO_2$-Ag-TiO_2 nanofluid produces enhanced thermal conductivity relative to $CoFeO_2$ unitary (mono) and $CoFeO_2$-Ag hybrid nanofluids.
12) The trihybrid $CoFeO_4$-Ag-TiO_2 nanofluid produces highest tangential skin friction values as compared to the other nanofluids

The present study has revealed some interesting characteristics of metallic ternary hybrid nanofluids in magnetic nanomaterial swirl coating fluid dynamics. Future investigations may consider alternative combinations of both metallic (e. g. zinc, gold, manganese etc) and carbon-based nanoparticles (e. g. diamond, graphene, graphite etc) and will be communicated 1imminently. Of course, the present methodology has been limited to similarity-based solutions. Future investigations can consider fully 3-D simulations using computational fluid dynamics for full visualization of the flow characteristics including vorticity.

ACKNOWLEDGMENTS

The authors are grateful to both reviewers for their comments which have served to improve the quality and clarity of the present work.

REFERENCES

[1] Von Kármán, Th. "Uber laminare und turbulente Reibung." *Z. Angew. Math. Mech.* 1, (1921), 233-252.

[2] W.G. Cochran, The flow due to a rotating disc, in: *Mathematical Proceedings of the Cambridge Philosophical Society*, 30, (1934), 365–375.

[3] J. T. Stuart, on the effects of uniform suction on the steady flow due to a rotating disk, The *Quarterly Journal of Mechanics and Applied Mathematics*, 7(4), (1954), 446–457.

[4] N. Gregory, J.T. Stuart, and W.S. Walker, On the stability of three-dimensional boundary layers with applications to the flow due to a rotating disk. *Philos Trans Roy Soc London Ser A*, 248, (1955), 155–199.

[5] E. Beton, On the flow due to a rotating disk, *Journal of Fluid Mechanics*, 24(4), (1966), 781-800.

[6] A. Mehmood**,** Asif Ali, H. S. Takhar, O. Anwar Bég, M.N. Islam and L.S. Wilson, Unsteady Von Kármán swirling flow: analytical study using the Homotopy Method, *Int. J. Applied Mathematics and Mechanics*, 6(2) , (2010), 67 – 84.

[7] S. Balachandar and C.L. Streett, Numerical simulation of transition in a rotating disk flow. In: Hussaini, M.Y., Voigt, R.G. (eds) *Instability and Transition. ICASE/ NASA LaRC Series. Springer, New York, NY* (1990).

[8] N. Kelson, and A. Desseaux, Note on porous rotating disk flow, *Aust. N. Z. Ind. Appl. Math. J.*, 42, (2000), 837–855.

[9] H.A. Jasmine and J.S.B. Gajjar, Absolut and convective instabilities in the incompressible boundary layer on a rotating disk with a temperature-dependent viscosity, *Int. J. Heat Mass Transfer*, 48, (2005), 1022–1037.

[10] Nguyen, Anh Ngoc, et al. "Spin coating and micro-patterning optimization of composite thin films based on PVDF." *Materials* 13(6), (2020), 1342.

[11] Wu, L.: Thermal effects on liquid film dynamics in spin coating. *Sens. Actuators A* 134, (2007), 140–145.

[12] B S Dandapat and G C Layek, Spin coating in the presence of a transverse magnetic field and non-uniform rotation: a numerical study, *J. Phys. D: Appl. Phys.* 32, (1999), 2483.

[13] R Aslam and W González-Viñas, Pattern formation in spin-coating of hybrid colloids in different magnetic field configurations, *J. Phys. D: Appl. Phys.* 52, (2019), 344001.

[14] A.N. Corpus-Mendoza *et al.*, Use of magnetic fields for surface modification of PbI_2 layers to increase the performance of hybrid perovskite solar cells, *J. Electronic Materials*; 49(5), (2020), 3106-3113.

[15] E.M. Sparrow and R.D. Cess, Magnetohydrodynamic flow and heat transfer about a rotating disk. J Appl Mech., 29, (1962), 181–187.

[16] T. Kakutani, Hydromagnetic flow due to a rotating disk, *Journal of Physical Society of Japan*, 17, (1962), 1496–1506.

[17] H.P. Pao, Magnetohydrodynamic flows over a rotating disk. *AIAA J.*, 6, (1968), 1285-1291.

[18] M. Turkyilmazoglu, Resonance instabilities in the boundary-layer flow over a rotating-disk under the influence of a uniform magnetic field, *J. Eng Math.*, 59, (2007), 337–350.

[19] M. Turkyimazoglu, Primary instability mechanisms on the magnetohydrodynamic boundary layer flow over a rotating disk subject to a uniform radial flow, *Physics of Fluids*, 21, (2009), 074103.

[20] A. Nakayama and C. D. Ebinuma, Transient non-Darcy forced convective heat transfer from a flat plate embedded in a fluid-saturated porous medium, *International Journal of Heat and Fluid Flow,* 11 (3), (1990), 249-253.

[21] Bég, O. Anwar, et al. "Transient Couette flow in a rotating non-Darcian porous medium parallel plate configuration: network simulation method solutions." *Acta Mechanica* 200(3-4), (2008), 129-144.

[22] Zhang, Lijun, et al. "Numerical study of natural convection dissipative electro-magnetic non-Newtonian flow through a non-Darcy channel." *ZAMM-Journal of Applied Mathematics and Mechanics/Zeitschrift für Angewandte Mathematik und Mechanik* 102(10), (2022), e202100608.

[23] H.A. Attia, Steady flow over a rotating disk in porous medium with heat transfer, *Nonlinear Analysis: Model. Control,* 14(1), (2009), 21–26.

[24] M.M. Rashidi, S.A. Mohimanian Pour, T. Hayat and S. Obaidat, Analytic approximate solutions for steady flow over a rotating disk in porous medium with heat transfer by homotopy analysis method, *Computers & Fluids*, 54, (2012), 1-9.

[25] O. Anwar Bég, K. Abdel Malleque and M.N. Islam, Modelling of Ostwald-deWaele non-Newtonian flow over a rotating disk in a non-Darcian porous medium, *Int. J. Applied Mathematics and Mechanics*, 8 (13), (2012), 46-67.

[26] R. Yu *et al.,* Ultrafast radiative heat transfer, *Nature Communications*, 8(2), (2017).

[27] S.G. Castillo-López, Enhancing near-field radiative heat transfer by means of superconducting thin films, I*nternational Journal of Heat and Mass Transfer*, 182, (2022), 121922.

[28] Viskanta, R. "Radiation heat transfer in materials processing and manufacturing." *Energy and the Environment*. Dordrecht: Springer Netherlands, (1999), 101-112.

[29] O. Anwar Bég, J. Zueco and L. M. López-Ochoa, Network numerical analysis of optically-thick hydromagnetic slip flow from a porous spinning disk with radiation flux, variable thermophysical properties and surface injection effects, *Chemical Engineering Communications*, 198(3) (2011), 360-384.

[30] Cattaneo C., A form of heat conduction equation which eliminates the paradox of instantaneous propagation. *Compte Rendus*, 247, (1958), 431–433.

[31] Özisik, M.N. and Tzou, D.Y.: On the wave theory in heat conduction. *ASME J. Heat Transfer*, 116, (1994), 526–535.

[32] T. Sanderson, C. Ume, and J. Jarzynski, Hyperbolic heat conduction effects caused by temporally modulated laser pulses, *Ultrasonics*, 33, (1995), 423–427.

[33] Maurer, M. J., Thompson, H. A., Non-Fourier effects at high heat flux, *ASME J. Heat Transfer*, 95, (1973), 284-286.

[34] Vedavarz, A., Kumar, S. and Moallemi, M.K., Significance of Non-Fourier heat waves in conduction, *ASME J. Heat Transfer*, 116, (1994), 116-224.

[35] Yang, H.Q., Non-Fourier effect on heat conduction during welding, *Int. J. Heat Mass Transfer*, 34, (1991), 2921-2924.

[36] X. Zhang *et al*, Thermomechanical coupling of non-Fourier heat conduction with the C-V model: thermal propagation in coating systems, *J. Thermal Stresses*, 38, (2015), 1104-1117.

[37] Alamri, Sultan Z., et al. "Effects of mass transfer on MHD second grade fluid towards stretching cylinder: a novel perspective of Cattaneo–Christov heat flux model." *Physics Letters A* 383(2-3), (2019), 276-281.

[38] Shehzad, S. A., et al. "Cattaneo-Christov heat flux model for Darcy-Forchheimer flow of an Oldroyd-B fluid with variable conductivity and non-linear convection." *Journal of Molecular Liquids* 224, (2016), 274-278.

[39] Hafeez, A., Khan, M., & Ahmed, J. Thermal aspects of chemically reactive Oldroyd-B fluid flow over a rotating disk with Cattaneo–Christov heat flux theory. *Journal of Thermal Analysis and Calorimetry*, (2020), 1-11.

[40] S.R. Mishra, M. Shamshuddin, O. Anwar Bég, Ali Kadir, Numerical study of heat transfer and viscous flow in a dual rotating extendable disk system with a non-Fourier heat flux model, *Heat Transfer,* 48 (1), (2019), 435-459.

[41] Choi, S. US, and Jeffrey A. Eastman. *Enhancing thermal conductivity of fluids with nanoparticles*. No. ANL/MSD/CP-84938; CONF-951135-29. Argonne National Lab. (ANL), Argonne, IL (United States), 1995.

[42] Q.Z. Xue, Model for thermal conductivity of carbon nanotube-based composites, *Phys. B Condens. Matter*, 368, (2005), 302–307.

[43] X. Wang, X. Xu, and S.U.S. Choi, Thermal conductivity of nanoparticle-fluid mixture, *AIAA J. Thermophys. Heat Transfer*, 13, (1999), 474–480.

[44] V. Trisaksri and S.J.R. Wongwises, Critical review of heat transfer characteristics of nanofluids, *Renew. Sust. Energ. Rev.*, 11 (3), (2007), 512–523.

[45] S. Murshed, K. Leong and C.J. Yang, Thermophysical and electrokinetic properties of nanofluids–a critical review, *Appl. Therm. Eng.*, 28, (2008), 2109–2125.

[46] Kumar, Aditya, et al. "Applications of nanofluids." *Thermal Characteristics and Convection in Nanofluids* (2021), 207-223.

[47] N. Bachok, A. Ishak and I. Pop, Flow and heat transfer over a rotating porous disk in a nanofluid, *Physica B*, 406(9), (2011), 1767–1772.

[48] J. Andrews and S.A. Devi, Nanofluid Flow over a rotating disk with prescribed heat flux. *Mapana-J. Sci.*, 11(3), (2012), 77–92.

[49] M.M. Rashidi, S. Abelman and N. Freidooni Mehr, Entropy generation in steady MHD flow due to a rotating porous disk in a nanofluid, *International Journal of Heat and Mass Transf.*, 62, (2013), 515-525.

[50] C. Yin, L. Zheng, C. Zhang and X. Zhang, Flow and heat transfer of nanofluids over a rotating disk with uniform stretching rate in the radial direction, *Propulsion Power Res.*, 6(1), (2017),25–30.

[51] Ahmad, Latif, Jawad Ahmed, and Awais Ahmed. "Thermal energy transport in thin film flow of nanofluid over a decelerating rotating disk." *Proceedings of the Institution of Mechanical Engineers, Part E: Journal of Process Mechanical Engineering* 236(2), (2022), 491-499.

[52] M. Khan, W. Ali and J. Ahmed, A hybrid approach to study the influence of Hall current in radiative nanofluid flow over a rotating disk, *Appl Nanosci.*, 10, (2020), 5167–5177.

[53] M. Khan, J. Ahmed, and W. Ali, Thermal analysis for radiative flow of magnetized Maxwell fluid over a vertically moving rotating disk, *J Therm Analysis Calorim.*, 143, (2021), 4081–4094.

[54] Upadhya, S. Mamatha, et al. "Magnetohydrodynamic nonlinear thermal convection nanofluid flow over a radiated porous rotating disk with internal heating." *Journal of Thermal Analysis and Calorimetry* 143, (2021), 1973-1984.

[55] Alsallami, Shami AM, et al. "Numerical simulations for optimised flow of second-grade nanofluid due to rotating disk with nonlinear thermal radiation: Chebyshev spectral collocation method analysis." *Pramana* 96(2), (2022), 98.

[56] Umavathi, J. C., and O. Anwar Bég. "Computation of Von Karman thermo-solutal swirling flow of a nanofluid over a rotating disk to a non-Darcian porous medium with hydrodynamic/thermal slip." *Journal of Thermal Analysis and Calorimetry* (2021), 1-16.

[57] Bég, O. Anwar, et al. "Numerical investigation of Von Karman swirling bioconvective nanofluid transport from a rotating disk in a porous medium with Stefan blowing and anisotropic slip effects." *Proceedings of the Institution of Mechanical Engineers, Part C: Journal of Mechanical Engineering Science* 235(19), (2021), 3933-3951.

[58] Naveen Kumar R, Gowda RJ, Gireesha BJ, Prasannakumara BC. Non-Newtonian hybrid nanofluid flow over vertically upward/downward moving rotating disk in a Darcy-Forchheimer porous medium. *Eur. Phys. J. Special Topics*, 230 (5), (2021), 1227–1237.

[59] A. Tassaddiq *et al.*, Heat and mass transfer together with hybrid nanofluid flow over a rotating disk, *AIP Advances*, 10, (2020) 055317.

[60] Shoaib, Muhammad, et al. "MHD hybrid nanofluid flow due to rotating disk with heat absorption and thermal slip effects: an application of intelligent computing." *Coatings* 11(12), (2021), 1554.

[61] H. Waqas, U. Farooq, R. Naseem, S.Hussain and M. Alghamdi, Impact of MHD radiative flow of hybrid nanofluid over a rotating disk, *Case Studies in Thermal Engineering*, 26, (2021), 101015.

[62] Khan, M. Ijaz. "Transportation of hybrid nanoparticles in forced convective Darcy-Forchheimer flow by a rotating disk." *International Communications in Heat and Mass Transfer* 122, (2021), 105177.

[63] Kumar, Mahesh, and Pranab Kumar Mondal. "Irreversibility analysis of hybrid nanofluid flow over a rotating disk: Effect of thermal radiation and magnetic field." *Colloids and Surfaces A: Physicochemical and Engineering Aspects* 635, (2022), 128077.

[64] Mousavi, Seyed Mahdi, et al. "Zinc oxide–silver/water hybrid nanofluid flow toward an off-centered rotating disk using temperature-dependent experimental-based thermal conductivity." *Heat Transfer* 51(5), (2022), 4169-4186.

[65] Shahzad, Faisal, et al. "Second-order convergence analysis for Hall effect and electromagnetic force on ternary nanofluid flowing via rotating disk." *Scientific Reports* 12(1), (2022), 18769.

[66] Alshahrani, Saad, et al. "Numerical simulation of ternary nanofluid flow with multiple slip and thermal jump conditions." *Frontiers in Energy Research* 10, (2022), 967307.

[67] Shamshuddin, M. D., et al. "Radiation mechanism on dissipative ternary hybrid nanoliquid flow through rotating disk encountered by Hall currents: HAM solution." *Alexandria Engineering Journal* 65, (2023), 543-559.

[68] Mustafa, M. "MHD nanofluid flow over a rotating disk with partial slip effects: Buongiorno model." *International Journal of Heat and Mass Transfer* 108, (2017), 1910-1916.

[69] Acharya, N., et al. "Hydrothermal variations of radiative nanofluid flow by the influence of nanoparticles diameter and nanolayer." *International Communications in Heat and Mass Transfer* 130, (2022), 105781.

[70] Waini, Iskandar, Anuar Ishak, and Ioan Pop. "Multiple solutions of the unsteady hybrid nanofluid flow over a rotating disk with stability analysis." *European Journal of Mechanics-B/Fluids* 94, (2022), 121-127.

[71] Khan, Sohail A., T. Hayat, and A. Alsaedi. "Thermal conductivity performance for ternary hybrid nanomaterial subject to entropy generation." *Energy Reports* 8, (2022), 9997-10005.

[72] Elsebaee, Fayza Abdel Aziz, Muhammad Bilal, Samy Refahy Mahmoud, Mohammed Balubaid, Muhammad Shuaib, Joshua KK Asamoah, and Aatif Ali. "Motile micro-organism based trihybrid nanofluid flow with an application of magnetic effect across a slender stretching sheet: Numerical approach." *AIP Advances* 13, no. 3 (2023).

[73] Al-Mubaddel, Fahad S., F. M. Allehiany, Taher A. Nofal, Mohammad Mahtab Alam, Aatif Ali, and Joshua Kiddy K. Asamoah. "Rheological model for generalized energy and mass transfer through hybrid nanofluid flow comprised of

magnetized cobalt ferrite nanoparticles." *Journal of Nanomaterials* 2022 (2022): 1-11.

[74] Ramasundaram, Subramaniyan, et al. "Direct preparation of nanoscale thin films of poly (vinylidene fluoride) containing β-crystalline phase by heat-controlled spin coating." *Macromolecular Chemistry and Physics* 209(24), (2008), 2516-2526.

[75] Salawu, S. O., M. D. Shamshuddin, and O. Anwar Bég. "Influence of magnetization, variable viscosity and thermal conductivity on Von Karman swirling flow of H2O-FE3O4 and H2O-Mn-ZNFe2O4 ferromagnetic nanofluids from a spinning disk: Smart spin coating simulation." *Materials Science and Engineering: B* 279, (2022), 115659.

[76] Wouters, Jelle, *et al.* "Preparing polymer films doped with magnetic nanoparticles by spin-coating and melt-processing can induce an in-plane magnetic anisotropy." *Journal of Applied Physics* 109(7), (2011).